

1 **The riddle of eastern tropical Pacific ocean oxygen levels : the role of the supply by**
2 **intermediate depth waters.**

3

4 Olaf Duteil (oduteil@geomar.de)(1), Ivy Frenger(1), Julia Getzlaff(1)

5 (1) GEOMAR, Kiel, Germany

6

7 **Abstract**

8 Observed Oxygen Minimum Zones (OMZs) in the tropical Pacific ocean are located above
9 intermediate depth waters (IDW). Typical climate models do not represent correctly IDW properties
10 and are characterized by a too deep reaching OMZ. We test here the role of the IDW on the
11 misrepresentation of oxygen levels in a heterogeneous subset of ocean models characterized by a
12 horizontal resolution ranging from 0.1° to 2.8°. First, we show that forcing the extra tropical
13 boundaries (30°S/N) to observed oxygen values results in a significant increase of oxygen levels in
14 the intermediate eastern tropical region. Second, the equatorial intermediate current system (EICS)
15 is a key feature connecting the western and eastern part of the basin. Typical climate models lack
16 in representing crucial aspects of this supply at intermediate depth, as the EICS is basically absent
17 in models characterized by a resolution lower than 0.25°. These two aspects add up to a “cascade
18 of biases”, that hampers the correct representation of oxygen levels at intermediate depth in the
19 eastern tropical Pacific Ocean and potentially future OMZs projections.

20

21 **1. Introduction**

22 Oxygen levels in the ocean are characterized by high values in the high latitudes and the
23 subtropical gyres, while concentrations decrease to close to zero in the tropical oceans in the
24 Oxygen Minimum Zones (OMZs). While OMZs are natural features, climate change is potentially
25 responsible for their expansion (Breitburg et al., 2018), leading to a reshaping of the ecosystems
26 and a potential loss of biodiversity.

27

28 Modelling oxygen levels is particularly challenging because of the complexity of the interactions
29 between biological respiration and physical transport (e.g Deutsch et al., 2014, Ito et al., 2013;
30 Duteil et al., 2014a,b, 2018, Oschlies et al., 2017). Climate models tend to overestimate the
31 volume of the OMZs (Cabre et al., 2015) and do not agree on the intensity and even sign of
32 oxygen future evolution (Oschlies et al., 2017). In order to perform robust projections there is a
33 need to better understand the processes at play that are responsible for the supply of oxygen to
34 the OMZ. We focus here on the Pacific ocean, where large OMZs are located in a depth range
35 from 100 to 900 m (Karstensen et al., 2008; Paulmier and Ruiz-Pino. 2009). Previous modelling
36 studies have shown that the tropical OMZ extension is at least partly controlled by connections with
37 the subtropical ocean (Duteil et al., 2014). In addition, the role of the equatorial undercurrent

38 (Shigemitsu et al., 2017; Duteil et al., 2018; Busecke et al., 2019), of the secondary Southern
39 Subsurface Countercurrent (Montes et al., 2014), of the interior eddy activity (Frenger et al., 2018),
40 have been previously highlighted. These studies focus on the mechanisms at play in the upper
41 oxygen levels (upper 500 m meter). The oxygen content below the core of the OMZ however plays
42 a significant role in setting the upper oxygen levels by diffusive (Duteil and Oschlies, 2009) or
43 vertical advective (Duteil, 2019) processes. Here, we focus specifically on the mechanisms
44 supplying oxygen toward the eastern tropical Pacific ocean at intermediate depth (500 – 1500 m),
45 below the OMZ core.

46
47 The water masses occupying this intermediate depth layer (500 – 1500 m) (Emery, 2003) subduct
48 at high latitudes. (Karstensen et al., 2008). Oxygen solubility increases with lower temperatures,
49 thus waters formed in the Southern Ocean and in the North Pacific are characterized by high
50 oxygen values. In particular, the Antarctic Intermediate Water (AAIW) (Molinelli, 1981) ventilates
51 large areas of the lower thermocline of the Pacific Ocean (Sloyan and Rintoul., 2001) and is
52 characterized by oxygen values larger than 300 mmol.m^{-3} at subduction time (Russell and Dickson,
53 2003). The oxygenated core of the AAIW in the tropical Pacific is located at about 500-1200 m
54 depth at 40°S (Russell and Dickson, 2003) and with this at a depth directly below the depth of the
55 OMZs in the eastern Pacific; the Pacific AAIW mixes down to 2000 m depth with the oxygen poor
56 Pacific Deep Water (PDW) as determined by the OMP (Optimum Multiparameter) analysis (Pardo
57 et al., 2012; Carrasco et al., 2017). The oxygen rich ($> 200 \text{ mmol.m}^{-3}$ at 40°S) AAIW spreads from
58 its formation side in the Southern Ocean to the subtropical regions. The northern part of the Pacific
59 basin is characterized by the North Pacific Intermediate Water (NPIW) (Talley, 1993) confined to
60 the northern Pacific conversely to the AAIW, which spreads far northward as its signature reaches
61 15°N (Qu and Lindstrom., 2004). AAIW, NPIW and the upper part of the PDW are oxygenated
62 water masses occupying the lower thermocline between 500 and 1500 m depth. In this study we do
63 not specifically focus on the individual water masses, but rather on the water occupying the
64 intermediate water depth (500 – 1500 m) (Emery, 2003) of the subtropical and tropical ocean. We
65 will refer to the waters in this depth range as intermediate depth waters (IDW).

66
67 In the subtropics, the IDW (particularly the AAIW) circulates into the intermediate flow of the South
68 Equatorial Current and the New Guinea Coastal Undercurrent (Qu and Lindstrom, 2004) where it
69 retroflects in the zonal equatorial flows of the Southern Intermediate Countercurrent (SICC) and
70 Northern Equatorial Intermediate Current (NEIC) within about $\pm 2^\circ$ off the equator (Zenk et al.,
71 2005; Kawabe et al., 2010) (Fig 1). These currents are part of the Equatorial Intermediate Current
72 System (EICS) constituted by a complex system of narrow jets extending below 500 m in the lower
73 thermocline (Firing, 1987; Ascani et al., 2010; Marin et al. 2010; Cravatte et al., 2012, 2017;
74 Menesguen et al., 2019). While the existence of this complex jet system has been shown to exist in

75 particular using argo floats displacements (Cravatte et al., 2017) the spatial structure and variability
76 of the jets are still largely unknown. In addition, there is little knowledge about their role in
77 transporting properties such as oxygen.

78

79 The simulation of the supply of oxygen to the eastern tropical Pacific below the OMZ core is a
80 difficult task as it depends on the realistic simulation of the IDW properties (in particular the
81 oxygen content) and the IDW pathway (through the EICS). It is known that current climate models,
82 in particular CMIP5 (Coupled Model Intercomparison Project phase 5) models, have deficiencies in
83 correctly representing the IDW, and in particular the AAIW. They generally display too shallow and
84 thin IDW, with a limited equatorward extension compared to observations (Sloyan and
85 Kamenkovich, 2007; Sallee et al., 2013; Meijers, 2014; Cabre et al., 2015; Zhu et al., 2018 for the
86 south Atlantic ocean). Discrepancies in the simulated properties of IDW compared to observations
87 are due to a combination of a range of errors in the climate models, including in the simulation of
88 wind and buoyancy forcing, an inadequate representation of subgrid-scale mixing processes in the
89 Southern Ocean, and midlatitude diapycnal mixing parameterizations (Sloyan and Kamakovich,
90 2007; Zhu et al., 2018). In addition, the EICS is mostly lacking in coarse resolution models (Dietze
91 and Loeptien, 2013; Getzlaff and Dietze, 2013). Higher resolution (0.25° , $1/12^\circ$) configurations
92 partly resolve the EICS but with smaller current speeds than observed (Eden and Dengler, 2008;
93 Ascani et al., 2015). The mechanisms forcing the EICS are complex and still under debate (see the
94 review by Menesguen et al., 2019).

95

96 In this study we focus on the impact of IDW (and of the deficiencies in the representation of their
97 properties and transport) on the oxygen content in the eastern tropical Pacific in a set of model
98 simulations. Section 2 gives an overview of all models that we used as well as of the sensitivity
99 simulations. Next, we assess to which extent the IDW modulate (or drive) the oxygen levels in the
100 eastern tropical ($20^\circ\text{S} - 20^\circ\text{N}$; 160°W -coast) Pacific ocean in this set of models. The role of the
101 IDW depends i) on the oxygen content of the IDW in the lower thermocline of the subtropical
102 regions (section 3) and ii) on the zonal recirculation of the oxygen by the EICS toward the eastern
103 part of the basin (section 4). We conclude in section 5.

104

105 **2. Analyzed models and experiments**

106 2.1 Mean state

107 We analyze the mean state of the oxygen fields, OMZ, EICS of the following model experiments
108 (see Table 1), which previously have been used in recent studies focusing on the understanding of
109 the tropical oxygen levels mean state or variability :

110 - the NEMO (Nucleus for European Modelling of the Ocean) model (Madec et al., 2017) with a
111 resolution of 2° , refined meridionally to 0.5° in the equatorial region (NEMO2 configuration). The

112 circulation model is coupled to a simple NPZD (Nutrient Phytoplankton Zooplankton Detritus)
113 biogeochemical model that comprises 6 compartments (e.g used in Duteil et al., 2018; Duteil,
114 2019). The simulation has been forced by climatological forcings based on the Coordinated
115 Reference Experiments (CORE) v2 reanalysis (Normal Year Forcing) (Large and Yeager, 2009)
116 and integrated for 1000 years.

117 - the UVIC (University of Victoria) model (e.g used in Getzlaff et al., 2016; Oschlies et al., 2017), an
118 earth System Model (ESM) that has a horizontal resolution of 1.8° latitude x 3.6° longitude. The
119 experiment has been integrated for 10000 years. The biogeochemical model is a NPZD-type
120 model of intermediate complexity that describes the full carbon cycle (see Keller et al., 2012 for a
121 detailed description). This model is forced by monthly climatological NCAR/NCEP wind stress
122 fields.

123 - the GFDL (Geophysical Fluid Dynamics Laboratory) CM2-0 suite (Delworth et al., 2012; Griffies
124 et al., 2015, Dufour et al, 2015): the suite is based on the GFDL global climate model and includes
125 a fully coupled atmosphere with a resolution of approximately 50 km. It consists of three
126 configurations that differ in their ocean horizontal resolutions: GFDL1 with a nominal 1° resolution,
127 GFDL025 with a nominal 0.25° and GFDL01 with a nominal 0.1° resolution (e.g used in Frenger et
128 al., 2018 and Busecke et al., 2019 for studies on ocean oxygen). At simulation year 48, the
129 simplified ocean biogeochemistry model miniBLING is coupled to the models, with three prognostic
130 tracers, phosphate, dissolved inorganic carbon and oxygen (Galbraith et al., 2015). Due to the high
131 resolution of GFDL01, the integration time is limited. We here analyze simulation years 186 to 190.
132 All the models (NEMO2, UVIC, GFDL suite) are forced using preindustrial atmospheric pCO₂
133 concentrations.

134 Differences in model resolution but also in atmosphere forcings or spinup duration strongly impact
135 oxygen distribution (see Annex A). However, the heterogeneity of the configurations that we
136 analyze permits to determine whether the simulated oxygen distributions display systematic biases
137 / similar patterns.

138 The mean states of the oxygen distributions are discussed below in section 3.1 “IDW Oxygen
139 levels in models”.

140

141 2.2 Sensitivity simulations

142 In order to disentangle the different processes at play we perform two different sets of sensitivity
143 simulations using the NEMO model engine. NEMO allows to test effects of increasing the ocean
144 resolution and to integrate the model over a relatively long time span. All sensitivity experiments
145 are integrated for 60 years (1948 to 2007) using the CORE (Coordinated Ocean-Ice Reference
146 Experiments) v2 interannual (Large and Yeager, 2009) forcings. This time scale permits the

147 recirculation from the interior subtropical regions to the tropical area (as suggested in the model
148 study by SenGupta and England, 2007).

149

150 2.2.1 Forcing of oxygen to observed values in the subtropical regions

151 In the first set of experiments the focus is on the role of the lower thermocline oxygen content for
152 the ventilation of the eastern equatorial Pacific. We use NEMO2, the oceanic component of the
153 IPSL-CM5A (Mignot et al., 2013), that is part of CMIP5. NEMO2 shows mid-latitudes oxygen
154 biases consistent with CMIP5 models. We compare three experiments :

155 - NEMO2-REF: the experiment is integrated from 1948 to 2007 starting from the spinup state
156 described in 2.1.

157 - NEMO2-30S30N: the oxygen boundaries are forced to observed oxygen concentrations (WOA) at
158 the boundaries 30°N and 30°S: the mid-latitude oxygen levels in the IDW are therefore correctly
159 represented.

160 - NEMO2-30S30N1500M: same as NEMO2-30S30N; in addition oxygen is forced to observed
161 concentrations at the depth interface of 1500m, mimicking a correct oxygen state of the deeper
162 water masses (lower part of the AAIW, upper part of the PDW)

163

164 With the above three experiments we focus on the transport of IDW oxygen levels to the tropical
165 ocean and the OMZs. The respiration rate (oxygen consumption) is identical in NEMO2-REF,
166 NEMO2-30S30N and NEMO2-30S30N1500M in order to avoid compensating effects between
167 supply and respiration that depend on biogeochemical parameterizations (e.g Duteil et al., 2012).
168 We aim to avoid such compensating effects to ease interpretation and be able to focus on the role
169 of the physical transport. The sensitivity of tropical IDW oxygen to subtropical and deep oxygen
170 levels is discussed in section 3.2

171

172 2.2.2 Conservative Tracer Release in oxygenated waters

173 In a second set of experiments, we assessed the effect of a resolution increase on the transport of
174 a conservative tracer. To do this, we used a 0.5° (NEMO05) and a higher resolution 0.1°
175 (NEMO01) configuration of the NEMO model engine (Table 1) to examine the transport of
176 oxygenated IDW from the subtropical regions into the oxygen deficient tropics. NEMO01 is a
177 configuration based on NEMO05 and where a 0.1° two-way nest has been embedded in the
178 whole Pacific Ocean, from 49°S to 31°N (Czeschel et al, 2011). In these experiments, we initialized
179 the regions with climatological (WOA) oxygen levels greater than 150 mmol.m⁻³ with a value of 1
180 (and 0 when oxygen was lower than 150 mmol.m⁻³). In the model simulations, the tracer is subject
181 to the same physical processes as other physical and biogeochemical tracers, i.e. advection and
182 diffusion but it does not have any sources and sinks. The experiments have been integrated for 60
183 years (1948 – 2007) using realistic atmospheric forcing (COREv2). NEMO05 and NEMO01 display

184 a similar upper ocean circulation (Fig 5) but NEMO05 does not simulate a developed EICS in
185 contrast to NEMO01.

186

187 In order to complement the tracer experiment we performed Lagrangian particle releases.
188 Lagrangian particles allow to trace the pathways of water parcels due to the resolved currents, and
189 to track the origin and fate of water parcels. They are not affected by subgrid scale diffusive and
190 advective processes. The particles are advected offline with 5 days mean of the NEMO05 and
191 NEMO01 currents. The NEMO01 circulation fields have been interpolated to the NEMO05 grid in
192 order to allow a comparison of the large scale advective patterns between NEMO01 and
193 NEMO05. We used the ARIANE tool (Blanke and Raynaud, 1997). A first particle release has been
194 performed in the eastern tropical OMZ at 100°W in the tropical region between 5°S - 5°N, a second
195 release has been performed in the western part of the basin at 160°E. The particles have been
196 released in the lower thermocline at 1000 m and integrated backward in time from 2007 to 1948 in
197 order to determine their pathways and their location of origin. We released 120 particles every 5
198 days during the last year of the experiment, for a total of 8760 particles. The transport by the EICS
199 is discussed in section 4.2 (tracers levels and Lagrangian pathways).

200

201 **3. Intermediate water properties and oxygen content**

202 3.1. IDW Oxygen levels in models

203 The IDW subducted in mid/high latitudes are highly oxygenated waters. As part of the deficient
204 representation of IDW, the subducted “oxygen tongue” (oxygen values up to 240 mmol.m⁻³) is not
205 reproduced in most of the models part of CMIP5 (Fig 8 from Cabre et al., 2015, Fig 4 from Takano
206 et al., 2018) and in the models analyzed here (Fig 2a), with an underestimation of about 20-60
207 mmol.m⁻³ (NEMO2, GFDL1, GFDL025, GFDL01). UVIC, a coarse resolution model, shows
208 oxygenated waters in the lower thermocline at mid latitudes (30°S-50°S); the oxygenation however
209 likely arises due to a too large vertical diffusion from the mixed layer rather than by an accurate
210 representation of the water masses.

211

212 GFDL01, even though still biased low, presents larger oxygen values than the coarser resolution
213 models GFDL1, GFDL025 and NEMO2. A possible explanation is a better representation of the
214 water masses and in particular the AAIW in eddy-resolving models (Lackhar et al., 2009).

215

216 The IDW oxygen maximum is apparent at 30°S throughout the lower thermocline (600 – 1000 m) in
217 observations (Fig 2b), consistent with the circulation of IDW with the gyre from the mid/high latitude
218 formation regions towards the northwest in subtropical latitudes, and followed by a deflection of the
219 waters in the tropics towards the eastern basin. This oxygen peak is missing in all the models
220 analyzed here.

221

222 Consistent with the low oxygen bias of models at subtropical latitudes (Fig 2b), models also feature
223 a bias in the tropical ocean (20°S-20°N) by 20 – 50 mmol.m⁻³ (Fig 2a, Fig 2c) at intermediate
224 depths in the eastern part of the basin (similarly to CMIP5 models, as shown by Cabre et al.,
225 2015). The basin zonal average of the mean oxygen level in the lower thermocline layer (500 -
226 1500m) at 30°S and in the eastern part of the basin (average 20°S – 20°N, 160°W-coast; 500-1500
227 m) are positively correlated (Pearson correlation coefficient R=0.73) (Fig 2d, Annex A), suggesting
228 that the oxygen levels in the tropical pacific ocean are partly controlled by extra-tropical oxygen
229 concentrations at intermediate depths and the associated water masses.

230

231 The models presenting the poorest oxygenated water at 30°S display the largest volume of OMZs
232 (GFDL025 and GFDL1), though the negative correlation (Pearson correlation coefficient R=-0.52)
233 is less pronounced between the volume of the OMZs and the mean oxygen levels in the layer 500 -
234 1500 m at 30°S (Fig 2e). Reasons for this weaker correlation are due to the OMZs being a result of
235 several processes next to oxygen supply by IDW, e.g, vertical mixing with other water masses
236 (Duteil et al., 2011), isopycnal mixing in the upper thermocline (Gnanadesikan et al., 2013; Bahl et
237 al., 2019), supply by the upper thermocline circulation (Shigemitsu et al., 2017; Busecke et al.,
238 2019). A correlation, even weak, suggests a major role of the IDW in regulating the OMZ volume.

239

240 In order to better understand the role of IDW entering the subtropical domain from higher latitudes
241 for the oxygen levels in the eastern tropical Pacific Ocean, we perform sensitivity experiments (see
242 2.2.1) in the following.

243

244 3.2 Sensitivity of tropical IDW oxygen to subtropical and deep oxygen levels

245 3.2.1 Oxygen levels in the lower thermocline

246 The difference of the experiments NEMO2-30S30N – NEMO2-REF (average 1997-2007) (Fig 3c,d)
247 allows to quantify the effect of model biases of IDW at mid latitudes (30°N/30°S) on tropical oxygen
248 levels. As we restore oxygen to observed levels at 30°S/°N (see 2.2.1), the difference between
249 both experiments shows a large anomaly in oxygen levels at 30°S (more than 50 mmol.m⁻³) at
250 lower thermocline level (500 – 1500 m) corresponding to the missing deep oxygen maximum,
251 located in the IDW. The northern negative anomaly results from a deficient representation of the
252 north Pacific OMZ, i.e., modeled oxygen is too high for NPIW. The northern low and southern high
253 anomalies spread towards the tropics at intermediate depth. A fraction of the positive oxygen
254 anomaly recirculates at upper thermocline level due to a combination of upwelling and zonal
255 advection by the tropical current system (for instance the EUC at thermocline level is a major
256 supplier of oxygen as shown in observations by Stramma et al., 2010 and in ocean models by
257 Duteil et al., 2014, Busecke et al., 2019).

258

259 The difference NEMO2-30S30N1500M – NEMO2-30S30N (Fig 3e,f) shows a deep positive
260 anomaly in oxygen, as oxygen levels are lower than in observations by 30-40 mmol.m⁻³ in the
261 eastern tropical regions. This anomaly is partially transported into the IDW (500 - 1500 m). It shows
262 that a proper representation of the deep oxygen levels (> 1500 m) is important for a realistic
263 representation of the lower thermocline and OMZs. Causes of the oxygen bias of the deeper water
264 masses are beyond the scope of this study but may be associated with regional (tropical) issues,
265 such as an improper parameterization of respiration (e.g a too deep remineralisation) (Kriest et al.,
266 2010), or a misrepresentation of deeper water masses.

267

268 3.2.2 Oxygen budget and processes

269 To assess the processes that drive the oxygen content of the (sub)tropical lower thermocline, we
270 analyzed the oxygen budget in NEMO2-REF and NEMO2-30S30N, NEMO30S30N1500M. The
271 budget is computed as an average between 500 and 1500m and shown in Fig 3g and Fig.4.

272

273 The oxygen budget is :

$$274 \frac{\delta O_2}{\delta t} = Adv_x + Adv_y + Adv_z + Diff_{Dia} + Diff_{Iso} + SMS$$

275 where Adv_x, Adv_y, Adv_z , are respectively the zonal, meridional and vertical advection terms, $Diff_{dia}$
276 and $Diff_{iso}$ are the diapycnal and isopycnal diffusion terms. SMS (Source Minus Sink) is the
277 biogeochemical component (i.e below the euphotic zone this is only respiration)

278

279 In NEMO2-REF, the physical oxygen supply is balanced by the respiration. The oxygen supply in
280 the model is divided into advection, i.e., oxygen transport associated with volume transport, and
281 isopycnal diffusion, i.e., subgrid scale mixing processes that homogenize oxygen gradients (Fig
282 4a). Diapycnal diffusion is comparatively small and can be neglected.

283

284 The supply of oxygen from the high latitudes toward the tropical interior ocean is constituted by
285 several processes acting concomitantly : isopycnal diffusion transfers oxygen from the oxygen-rich
286 gyres to the poor oxygenated regions (see Fig 1). The lower branches of the subtropical gyres
287 transport the oxygen from the eastern to the western part of the basin. Downwelling from the
288 oxygen-rich mixed layer supplies the interior of the subtropical gyres. At the equator, the EICS
289 transport westward oxygen-poor water originating in the eastern side of the basin (Fig 4a). The
290 meridional advection term transports oxygen originating from the subtropics in the tropical regions,
291 which is upwelled.

292

293 Forcing oxygen levels in NEMO2-30S30N at 30°S and 30°N creates an imbalance between
294 respiration (which remains identical in NEMO2-REF and NEMO2-30S30N) and supply. This
295 imbalance is most apparent in the tropics by an increase (south) or decrease (north) of isopycnal
296 diffusion (Fig 3g, Fig 4b). Changes in the advective terms are found along the equator: as the
297 vertical gradient of oxygen decreases (the intermediate ocean being more oxygenated), the vertical
298 supply from the upper ocean decreases in the south (increases in the north) subtropical gyre and
299 decreases at the equator (Fig 4b). The meridional oxygen gradient between the southern
300 subtropical gyre and the equator strengthens, and so does the meridional transport from the
301 subtropics to the equator, partly by the western boundary currents. The changes in zonal transport
302 are comparatively small.

303

304 In the experiment NEMO2-30S30N1500, in complement to the isopycnal propagation of the
305 subtropical anomaly, the deep (> 1500 m) oxygen anomaly is upwelled in the eastern equatorial
306 (500 – 1500 m) part of the basin (see Fig 3g). The transport due to advective terms strongly
307 increases, mostly due to an increase in vertical advection. This is consistent with the analysis by
308 Duteil (2019) who showed that vertical advection is the dominant process to supply oxygen from
309 the lower to the upper thermocline in the equatorial eastern Pacific Ocean in a similar NEMO2
310 configuration.

311

312 This simple set of experiments already shows that in climate models oxygen in the lower
313 thermocline (500 – 1500 m) tropical ocean are partially controlled by properties of IDW that enter
314 the tropics from higher latitudes. This presumably also applies to other (biogeochemical) tracers.
315 IDW oxygen propagates equatorward mostly by small scale isopycnal processes and the western
316 boundary currents. Further, upwelling in the tropics from deeper ocean layers (Pacific Deep Water,
317 partially mixed with the lower IDW) play an important role. We will examine more closely in the
318 following the representation and the role of the EICS in supplying oxygen toward the eastern
319 Pacific Ocean.

320

321 **4. Equatorial intermediate current system and oxygen transport**

322 4.1 Structure of the currents in the upper 2000 m in observations and models

323 The current structure of the models analyzed in this study (see section 2.1, Table 1) is shown in
324 Fig 5. In the mixed layer, the broad westward drifting South and North Equatorial Currents (SEC,
325 NEC) characterize the equatorial side of subtropical gyres. In the thermocline, the eastward flowing
326 equatorial undercurrent (EUC), flanked by the westward flowing south and north counter currents
327 are present in all models. This upper current structure is well reproduced (i.e the spatial structure
328 and intensity are consistent with observations) across the different models (see 2.1 “Model
329 analyzed”) compared to observations. Previous studies already discussed the upper thermocline

330 current structure in the GFDL models suite (Busecke et al., 2019), NEMO2 and NEMO05 (e.g
331 Izumo, 2005, Lübbecke et al., 2008), UVIC (Loeptien and Dietze, 2013); the upper thermocline will
332 not be further discussed in this study.

333

334 At intermediate depth, in the observations, a relatively strong (about 0.1 ms^{-1}) westward flowing
335 Equatorial Intermediate Current (EIC) is present below the EUC at about 400-600 m depth (Marin
336 et al., 2010). A complex structure of narrow and vertically alternating jets every 200 m, so-called
337 Equatorial Deep Jets (EDJ), extends below the EIC till 2000 m (Firing, 1987; Cravatte et al., 2012).
338 Laterally to the EIC, in the upper thermocline, the Low Latitude Subsurface Countercurrents
339 (LLSC) are observed. They include the North and South Subsurface Counter Currents (NSCC and
340 SSCC), located around $5^{\circ}\text{N}/5^{\circ}\text{S}$, and a series of jets between $5^{\circ}\text{N}/\text{S}$ and $15^{\circ}\text{N}/\text{S}$ (in particular the
341 Tsuchiya jets in the southern hemisphere, described by Rowe et al., 2000). Below the LLSCs, the
342 Low Latitude Intermediate Currents (LLICs) include a series of westward and eastward zonal jets
343 (500–1500-m depth range) alternating meridionally from 3°S to 3°N ; the North and South
344 Intermediate Countercurrents (NICC and SICC) flow eastward at 1.5° – 2° on both flanks of the
345 lower EIC. The North and South Equatorial Intermediate Currents (NEIC and SEIC) flow westward
346 at about 3° (Firing, 1987). A detailed schematic view of the tropical intermediate circulation is
347 shown in a recent review by Menesguen et al. (2019) and in Fig 1.

348

349 In coarse resolution models, the intermediate current system is not developed and sluggish (even
350 missing in UVIC and GFDL1). NEMO2 and NEMO05 display a “primitive” EICS as the LLSCs are
351 not represented. High resolution models (GFDL025, GFDL01, NEMO01) display a more realistic
352 picture, even if the mean velocity is still weaker than in observations (smaller than $5 \text{ cm}\cdot\text{s}^{-1}$), where
353 it reaches more than 10 cm^{-1} at 1000 m (Ascani et al., 2010; Cravatte et al., 2017). An interesting
354 feature is that the jets are broader and faster in NEMO01 than in GFDL01. Possible causes
355 include a different wind forcing, mixing strength or topographic features as all these processes play
356 a role in forcing the intermediate jets (see the review by Menesguen et al., 2019). The intermediate
357 currents are less coherent vertically in NEMO01 than in GFDL01, due to their large temporal
358 variability in NEMO01. A strong seasonal and interannual variability of the EICS has been
359 observed that displays varying amplitudes and somewhat positions of the main currents/jets
360 (Firing, 1998; Gouriou et al., 2006; Cravatte et al., 2017). A clear observational picture of the EICS
361 variability is however not yet available. Outside the tropics (in particular south of 15°S), the interior
362 velocity pattern is similar in coarse and high resolution models, suggesting a similar equatorward
363 current transport at intermediate depth in the subtropics, in for instance NEMO05 and NEMO01.

364

365 4.2 Transport by the EICS

366 4.2.1 Tracer spreading towards the eastern tropical Pacific

367 We released a conservative tracer in the subtropical domain in well oxygenated waters (see 2.2.2)
368 in a coarse (NEMO05) and a high resolution configuration (NEMO01). The tracer does not have
369 sources or sinks and is advected and mixed as any other model tracer and allows to assess the
370 transport pathway of tracer (such as oxygen) from oxygenated waters into the oxygen deficient
371 eastern tropical Pacific.

372

373 The importance of the ventilation by the oxygen rich waters, and in particular the IDW, is illustrated
374 by the tropical tracer concentration after 50 years (Fig 6a) of integration (mean 2002-2007).
375 Concentrations decrease from the release location to the northern part of the basin, where the
376 lowest values (below 0.1) are located in NEMO05 and NEMO01. The 0.1 isoline is however
377 located close to the equator in NEMO05 while it is found around 7°N in NEMO01. This feature is
378 associated with a pronounced tongue of high tracer concentration (> 0.2) between 5°N and 5°S in
379 NEMO01. Such a tongue is absent in NEMO05. The enhanced tracer concentration in the equatorial
380 region suggests a stronger zonal equatorial ventilation in NEMO01.

381

382 The preferential pathways of transport are highlighted by the determination of the transit time it
383 takes for the tracer to spread from the oxygen rich regions to the tropical regions. We define a
384 threshold called $t_{10\%}$ when the tracer reaches a concentration of 0.1 (Fig 6b) (similar to the
385 approach of SenGupta and England, 2007). $t_{10\%}$ highlights a faster ventilation of the equatorial
386 regions in NEMO01 compared to NEMO05, as $t_{10\%}$ displays a maximum value of 10 (western
387 part) to 30 years (eastern part) between 5°N/5°S in NEMO01 compared to 30 years to more than
388 50 years in NEMO05. The southern “shadow zone” is well individualized in NEMO01 compared to
389 NEMO05 as the oxygen levels are high in the equator in NEMO01, suggesting a strong transport
390 by the EICS. The value of $t_{10\%}$ increases linearly at intermediate depth at 100°W in NEMO05 from
391 20°S to the equator, suggesting a slow isopycnal propagation (consistent with the experiments
392 performed using NEMO2 in part 3.2). Conversely, the tracer accumulation is faster in the equatorial
393 regions than in the mid-latitudes in NEMO01, suggesting a large role of advective transport, which
394 is faster than the transport by diffusive processes.

395

396 4.2.2 Equatorial lower thermocline water mass origin

397 Lagrangian particles (see 2.2.3) allow us to understand the origin of the waters in the lower
398 thermocline. They also allow us to disentangle the transport of the resolved currents of the EICS
399 (advection) from subgrid scale mixing processes, i.e. to assess the processes responsible for the
400 equatorial ventilation. Two releases R1 and R2 have been performed in the eastern and western
401 part of the basin in order to assess the equatorial circulation in NEMO05 and NEMO01. A depth
402 horizon of 1000 m has been chosen as it is a depth where the equatorial intermediate current
403 system is relatively well developed in high resolution models and basically absent in coarse models

404 (see Fig 5). Our results are not sensitive to the choice of another depth horizon in the range of 500
405 - 1500 m

406

407 The release R1 (100°W, 5°N-5°S, 1000 m depth) is located in the larger intermediate eastern
408 tropical pacific (IETP) ocean region (160°W – coast / 10°N-10°S / 200 – 2000 m). The particles
409 originate close to the region of release (IETP) in 60 % of the cases in NEMO05 and 50 % of the
410 cases in NEMO01, at a time scale of 50 years (Fig 7a and 8b). In NEMO05, after 50 years, the
411 particles originating outside the IETP come either from the upper (0 – 200 m) ocean (5 %), deep
412 (> 2000 m) ocean (1%), higher (> 10°) latitudes (23 %), western (west of 160°W) part of the basin
413 (21 %) (Fig 8d). The largest difference between NEMO05 and NEMO01 is the much larger amount
414 of particles originating from the deep ocean in NEMO01 (8 % in NEMO01), suggesting the
415 presence of vertical recirculation cells at intermediate depths. Despite the stronger EICS in
416 NEMO01, the amount of particles originating from the western part of the basin is nearly identical
417 in NEMO01 and NEMO05 after 50 years of integration. The advection processes are however
418 faster in NEMO01, in particular the zonal advection. The relative difference between NEMO05 and
419 NEMO01 is particularly strong 15 years after the release (approximately corresponding to the t10%
420 at 1000 m at the equator in NEMO01), as already 10 % of the particles originate outside the IETP,
421 in regions where the oxygen levels are high, in NEMO01 while this fraction is close to 0 in
422 NEMO05.

423

424 The second release R2 (160°E, 5°N-5°S, 1000 m depth) is located in the intermediate western
425 tropical pacific (IWTP) ocean region (160°W – coast / 10°N-10°S / 200 – 2000 m) (Fig 7b). After 50
426 years, all the particles originate outside of the IWTP in NEMO01 (Fig 8c) (50 % originate in the
427 eastern basin, 23 % in the deep ocean, 24 % outside the equatorial band, 3 % in the upper 200 m)
428 (Fig 8e) while only 70 % of the particles originate outside the IWTP in NEMO05 (39 % in the
429 eastern basin, 27 % outside the equatorial band, 2 % in the deep ocean and 2 % in the upper
430 ocean).

431

432 The Lagrangian experiments show a generally stronger ventilation at intermediate depth in
433 NEMO01 due to the EICS, which reinforces the connections between western / eastern part of the
434 basin and the thermocline / deep ocean.

435

436 4.3 Model resolution and oxygen levels

437 The experiments discussed in 4.2 were not coupled with biogeochemical cycles for computational
438 cost reasons. In order to assess the robustness of our findings (EICS plays a large role in setting
439 tropical oxygen levels), we next analyze equatorial oxygen in a set of climate models similar to

440 CMIP models. To this end we use the GFDL model suite, characterized by a resolution increase
441 (GFDL1, GFDL025 and GFDL01 - see Table 1).

442

443 The striking difference between GFDL01 and GFDL025 / GFDL1 are the high oxygen levels in the
444 eastern part of the ocean below 1000 m in GFDL01 compared to GFDL025/GFDL1 (Fig 2). The
445 oxygen levels show weaker zonal gradient in GFDL01, consistent with the tracer experiment that
446 we performed in 4.2. and a more ventilated intermediate equatorial ocean. High values of mean
447 kinetic energy are associated with higher oxygen values (Fig 9). This is particularly clear in
448 GFDL01 at around 1500 m depth, where strong values of MKE are present and form the “bottom”
449 of the low oxygen volume (oxygen lower than 50 mmol.m⁻³). Conversely GFDL025 and GFDL1 do
450 not present high MKE values below 1000 m in the eastern part of the basin; the low oxygen volume
451 extends till depths greater than 2000 m. It suggests that intermediate currents participate in the
452 ventilation of the eastern tropical ocean and thus in limiting the vertical extension of the OMZ.

453

454 Oxygen levels do not increase linearly with the currents strength, i.e while currents strength
455 increase in GFDL1, GFDL025 and GFDL01, oxygen levels are relatively similar in GFDL1 and
456 GFDL025 (see Fig 5 and Fig 9). The relatively small net balance between large fluxes of
457 respiration and oxygen supply (Duteil et al., 2014) may be responsible for this behavior. If the
458 supply is slightly higher compared to the consumption by respiration, it will lead to an increase of
459 oxygen concentration. If it is slightly lower, the oxygen levels will decrease. A small difference in
460 supply (e.g slightly weaker currents) may therefore lead to a large difference in oxygen levels when
461 integrated over decades. For this reason, the impact of the EICS is more visible below 1000 m as
462 the respiration decreases following a power-law with depth (Martin et al., 1987) and is therefore
463 easier to offset even by a moderate oxygen supply.

464

465 Resolving explicitly the EICS results in a similar oxygen distribution to what Getzlaff and Dietze
466 (2013) (GD13) achieved with a simple EICS parameterization (Fig 9a): to compensate for the
467 “missing” EICS in UVIC, a coarse resolution model, they enhanced anisotropically the lateral
468 diffusivity in the equatorial region. The oxygen levels from UVIC GD13 are shown in blue contours
469 on top of the UVIC oxygen distribution (black) in Fig 9. Implementing this approach tends to
470 homogenize oxygen levels zonally, with an increase of the mean levels by 30-50 mmol.m⁻³ in the
471 eastern basin and a decrease of oxygen concentrations in the western basin. While this approach
472 may be useful to better represent the oxygen mean state, it however does not take in account the
473 potential variability and future evolution of the EICS.

474

475 **5. Summary and conclusions**

476 Intermediate Depth Waters (IDW) are subducted in the Southern Ocean and transported
477 equatorward to the tropics by isopycnal processes (Sloyan and Kamenskovich, 2007; Sallee et al.,
478 2013; Meijers, 2014). At lower latitudes they recirculate into the lower thermocline of the tropical
479 regions at 500 - 1500 m and into the EICS (Zenk et al., 2005; Marin et al., 2010; Cravatte et al.,
480 2012; 2017; Ascani et al., 2015; Menesguen et al., 2019) (see schema Fig 1). We show here that
481 the representation of this ventilation pathway is important to take into account when assessing
482 tropical oxygen levels and the extent of the OMZ in coupled biogeochemical circulation or climate
483 models. Particularly, we highlight two critical, yet typical, biases that hamper the correct
484 representation of the tropical oxygen levels.

485

486 5.1 Subducted IDW properties and tropical oxygen

487 First, the current generation of climate models, such as the CMIP5 models, show large deficiencies
488 in simulating IDW. Along with an unrealistic representation of IDW volume and properties when the
489 waters enter the subtropics, the models also lack the observed prominent oxygen maximum
490 associated with IDW. Restoring oxygen levels to observed concentrations at 30°S/30°N and at
491 1500 m depth in a coarse resolution model, comparable to CMIP5 climate models in terms of
492 resolution and oxygen bias, shows a significant impact on the lower thermocline (500 – 1500 m)
493 oxygen levels: a positive anomaly of 60 mmol.m⁻³ at midlatitudes translates into an oxygen
494 increase by 10 mmol.m⁻³ in tropical regions after 50 years of integration.

495

496 The equatorward transport of the anomaly in the subtropics is mostly due to isopycnal subgrid
497 scale mixing processes as shown by the NEMO2 budget analysis. It suggests that mesoscale
498 activity plays a major role in transporting IDW equatorward. In addition subsurface eddies may
499 transport oxygen westward from the eastern Pacific ocean toward the mid-Pacific ocean region
500 (Frenger et al., 2018, see their Fig 2).

501

502 5.2 IMW transport and Equatorial Intermediate Current System

503 Second, the Equatorial Intermediate Current System (EICS) is not represented in coarse
504 resolution models and only poorly represented in high resolution ocean circulation models (0.25°
505 and 0.1°), as its strength remains too weak by a factor of two (consistent with previous studies, e.g
506 Ascani et al., 2015). The EICS transports the IDW that occupies the lower thermocline (500 – 1500
507 m depth) and the recirculation of the IDW in the tropical ocean, as suggested by the observational
508 study of Zenk et al. (2005), and shown in our study.

509

510 We investigated the impact of the EICS on the oxygen supply with tracer release experiments: the
511 concentration of a conservative tracer that originates from the subtropical ocean, is, after 50 years,
512 30 % higher in the eastern equatorial (5°N-5S) Pacific in an ocean model with 0.1° resolution,

513 compared to an ocean model with 0.5 ° resolution. As the oxygen gradient along the equator is
514 similar to the gradient of the conservative tracer, we assume a similar enhancement of oxygen
515 supply by 30 % in the eastern equatorial Pacific at the same time scale. This means, if we account
516 for oxygen consumption due to respiration (about 1 mmol.m⁻³.yr⁻¹ between 5°N-5°S, see section
517 3.2), that the better resolved EICS in the higher resolution ocean leads roughly to higher
518 intermediate oxygen levels of 15 - 30 mmol.m⁻³ compared to the lower resolution ocean experiment
519 in a timescale of 50 years. Consistently, the 0.1°-ocean GFDL01 model displays oxygen
520 concentrations larger by about 30 mmol.m⁻³ in the eastern equatorial lower thermocline (500-1500
521 m) compared to the 1°-ocean GFDL1 configuration (with higher subtropical oxygen concentrations
522 of IWM of 15 mmol.m⁻³ in GFDL01 at 30°S)

523

524 We would like to highlight two potential implications of our finding of the important role of the EICS
525 for the Pacific eastern tropical oxygen supply: i) First, we have shown that the intermediate current
526 system EICS is important for the connection between the western and eastern Pacific Ocean at a
527 decadal / multidecadal time scale. This suggests that the EICS modulates the mean state and the
528 variability of the tropical oxygen in the lower thermocline, and subsequently the whole water
529 column by upwelling of deep waters. ii) Second, we have found an enhancement of the
530 connections between the equatorial deep ocean (> 2000 m) and the lower thermocline if the
531 resolution of a model is enhanced. This result is consistent with the studies of Brandt et al. (2011,
532 2012), who suggested, based on observational data and on an idealized model, that Equatorial
533 Deep Jets as part of the EICS (see Fig 1b) propagate their energy upward and impact the upper
534 ocean properties of the ocean, including their oxygen content. Taken this into account, we
535 hypothesize that the Pacific Deep Water has a larger role than previously thought in modulating the
536 intermediate and upper ocean properties.

537

538 A pragmatic approach to account for the missing EICS is to increase diffusion anisotropically, with
539 increased zonal mixing in the tropics (Getzlaff and Dietze, 2013). This parameterization mimics a
540 more vigorous EICS and improves the simulated shape of the OMZ in climate models. However,
541 the prominent bias of IDW in climate models, and therefore of the water masses entering the EICS
542 is not accounted for with this parameterization. Furthermore such a parameterization improves the
543 mean state but does not reproduce the variability of the EICS.

544

545 5.3 Implication for biogeochemical cycles

546 The IDW are an important important supplier of oxygen to the tropical oceans, but also of nutrients
547 (Palter et al., 2010) as well as anthropogenic carbon (e.g Kathiwala et al., 2012), which
548 accumulates in mode and intermediate waters of the Southern Ocean (Sabine et al., 2004;

549 Resplandy et al., 2013). The mechanisms that we discussed here may therefore play a role in
550 ocean carbon climate feedbacks on time scales of decades to a century.

551

552 This study shows that there is a need to look with greater care into IDW properties to understand
553 the tropical oxygen distribution in models, in particular in CMIP class models. As shown by
554 Kwiatkowski et al. (2020), CMIP6 models (typical horizontal resolution of 1°) do not agree on the
555 future change in tropical oxygen levels (mean 100 – 600m, their Fig 2). This may partly originate in
556 a misrepresentation of the properties of the IDW in the different models and the strength of the
557 connection between western and eastern Pacific Ocean. Simple analyses, similar to our Fig 2
558 (oxygen levels at 30°S and oxygen levels in the eastern tropical Pacific) and Fig 9 (Mean Kinetic
559 Energy at intermediate depth) may give some insight into the mechanisms at play. In addition,
560 analyses of experiments performed in the context of the High Resolution Model Intercomparison
561 Project (resolution greater than 0.25°) (Haarsma et al., 2016), part of CMIP6, will give a more
562 complete insight on whether a significant Equatorial Intermediate Current System develops at
563 higher resolution. While HighResMIP are not coupled with a biogeochemical module, velocity fields
564 are available at a monthly resolution, which allows to perform “offline” tracer or Lagrangian particle
565 experiments.

566

567 Finally, this study suggests that changes of the properties of the IDW may contribute to the still
568 partly unexplained deoxygenation of 5 mmol.m⁻³ / decade occurring in the lower thermocline of the
569 equatorial eastern Pacific Ocean (Schmidtko et al., 2017; Oschlies et al., 2018). In addition to an
570 oxygen decrease in tropical regions, Schmidtko et al. (2017) showed a decrease of oxygen levels
571 by 2-5 mmol.m⁻³ in the regions of formations of AAIW. Based on repeated cruise observations,
572 Panassa et al. (2018) highlighted an increase of the apparent oxygen utilization in the core of the
573 AAIW, together with a 5 % increase in nutrient concentrations from 1990 to 2014. The transport of
574 this modified AAIW, poorer in oxygen and richer in nutrients, toward the low latitudes both by small
575 scale processes (section 3) and at the equator by the EICS (section 4), may explain a significant
576 part of the occurring deoxygenation in the equatorial ocean. In addition to changes in the AAIW
577 properties, little is known about the variability and long term trend of the strength of the EICS, an
578 oceanic “bridge” between the western and the eastern part of the basin. After our first steps toward
579 assessing the role of extratropical oxygen characteristics and the zonal transport of waters at
580 intermediate depths for tropical oxygen concentration, a possible way forward to further assess this
581 cascade of biases could be to perform idealized model experiments in high resolution
582 configurations, aiming to assess both the effect of the observed change in the AAIW properties and
583 of a potential change of EICS strength on oxygen levels.

584

585

586 **Data and code availability**

587 The code for the Nucleus for European Modeling of the Ocean (NEMO) is available at:
588 <https://www.nemo-ocean.eu/>. The code for the University of Victoria (UVIC) model is available
589 at [:http://terra.seos.uvic.ca/model/](http://terra.seos.uvic.ca/model/). The Lagrangian particles ARIANE code is available at
590 <http://stockage.univ-brest.fr/~grima/Ariane/>. The Coordinated Ocean-ice Reference Experiments
591 (COREv2) dataset is available at: <https://data1.gfdl.noaa.gov/nomads/forms/core/COREv2.html>.
592 The experiments data is available on request.

593

594 **Authors contributions**

595 OD conceived the study, performed the NEMO model and ARIANE experiments and analyzed the
596 data. IF preprocessed and helped to analyze the GFDL data. JG preprocessed and helped to
597 analyze the UVIC data. All authors discussed the results and wrote the manuscript.

598

599 **Competing interest**

600 The authors declare that they have no conflict of interest.

601

602 **Acknowledgments**

603 This work is a contribution of the SFB754 “Climate-Biogeochemistry Interactions in the Tropical
604 Ocean”, supported by the Deutsche Forschungsgemeinschaft (DFG). The NEMO simulations were
605 performed at the North German Supercomputing Alliance (HLRN). We would like to thank Markus
606 Scheinert (research unit “Ocean Dynamics”, GEOMAR) for his technical support in compiling the
607 NEMO code and for providing the high resolution NEMO input files. We would like to thank GFDL
608 for producing the CM2-0 suite that involved a substantial commitment of computational resources
609 and data storage. J.G acknowledges support by the project "Reduced Complexity Models"
610 (supported by the Helmholtz Association of German Research Centres (HGF) – grant no. ZT-I-
611 0010). I.F. acknowledges the German Federal Ministry of Education and Research (BMBF) project
612 CUSCO (grant no. 03F0813A). O.D acknowledges the German Research Foundation (DFG) (grant
613 no. 434479332)

614

615 **References**

- 616 Ascani, F., Firing, E., Dutrieux, P., McCreary, J. P., & Ishida, A. (2010). Deep Equatorial Ocean
617 Circulation Induced by a Forced–Dissipated Yanai Beam. *Journal of Physical Oceanography*,
618 40(5), 1118–1142. doi:10.1175/2010jpo4356.1
- 619 Ascani, F., Firing, E., McCreary, J. P., Brandt, P., & Greatbatch, R. J. (2015). The Deep Equatorial
620 Ocean Circulation in Wind-Forced Numerical Solutions. *Journal of Physical Oceanography*, 45(6),
621 1709–1734. doi:10.1175/jpo-d-14-0171.1

622 Bahl, A., Gnanadesikan, A., & Pradal, M. A. (2019). Variations in Ocean Deoxygenation Across
623 Earth System Models: Isolating the Role of Parameterized Lateral Mixing. *Global Biogeochemical*
624 *Cycles*, 33(6), 703–724. doi:10.1029/2018gb006121

625 Blanke, B., & Raynaud, S. (1997). Kinematics of the Pacific Equatorial Undercurrent: An Eulerian
626 and Lagrangian Approach from GCM Results. *Journal of Physical Oceanography*, 27(6), 1038–
627 1053. doi:10.1175/1520-0485(1997)027<1038:kotpeu>2.0.co;2

628 Brandt, P., Funk, A., Hormann, V., Dengler, M., Greatbatch, R. J., & Toole, J. M. (2011).
629 Interannual atmospheric variability forced by the deep equatorial Atlantic Ocean. *Nature*,
630 473(7348), 497–500. doi:10.1038/nature10013

631 Brandt, P., Greatbatch, R. J., Claus, M., Didwischus, S.-H., Hormann, V., Funk, A., ... Körtzinger,
632 A. (2012). Ventilation of the equatorial Atlantic by the equatorial deep jets. *Journal of Geophysical*
633 *Research: Oceans*, 117(C12), n/a–n/a. doi:10.1029/2012jc008118

634 Breitburg, D., Levin, L. A., Oschlies, A., Grégoire, M., Chavez, F. P., Conley, D. J., ... Zhang, J.
635 (2018). Declining oxygen in the global ocean and coastal waters. *Science*, 359(6371), eaam7240.
636 doi:10.1126/science.aam7240

637 Busecke, J. J. M., Resplandy, L., & Dunne, J. P. (2019). The Equatorial Undercurrent and the
638 Oxygen Minimum Zone in the Pacific. *Geophysical Research Letters*, 46(12), 6716–6725.
639 doi:10.1029/2019gl082692

640 Cabré, A., Marinov, I., Bernardello, R., & Bianchi, D. (2015). Oxygen minimum zones in the tropical
641 Pacific across CMIP5 models: mean state differences and climate change trends. *Biogeosciences*,
642 12(18), 5429–5454. doi:10.5194/bg-12-5429-2015

643 Carrasco, C., Karstensen, J., & Farias, L. (2017). On the Nitrous Oxide Accumulation in
644 Intermediate Waters of the Eastern South Pacific Ocean. *Frontiers in Marine Science*, 4.
645 doi:10.3389/fmars.2017.00024

646 Cravatte, S., Kessler, W. S., & Marin, F. (2012). Intermediate Zonal Jets in the Tropical Pacific
647 Ocean Observed by Argo Floats. *Journal of Physical Oceanography*, 42(9), 1475–1485.
648 doi:10.1175/jpo-d-11-0206.1

649 Cravatte, S., Kestenare, E., Marin, F., Dutrieux, P., & Firing, E. (2017). Subthermocline and
650 Intermediate Zonal Currents in the Tropical Pacific Ocean: Paths and Vertical Structure. *Journal of*
651 *Physical Oceanography*, 47(9), 2305–2324. doi:10.1175/jpo-d-17-0043.1

652 Czeschel, R., Stramma, L., Schwarzkopf, F. U., Giese, B. S., Funk, A., and Karstensen, J. (2011),
653 Middepth circulation of the eastern tropical South Pacific and its link to the oxygen minimum zone,
654 *J. Geophys. Res.*, 116, C01015, doi:10.1029/2010JC006565

655 Delworth, T. L., Rosati, A., Anderson, W., Adcroft, A. J., Balaji, V., Benson, R., ... Zhang, R.
656 (2012). Simulated Climate and Climate Change in the GFDL CM2.5 High-Resolution Coupled
657 Climate Model. *Journal of Climate*, 25(8), 2755–2781. doi:10.1175/jcli-d-11-00316.1

658 Dietze, H., & Loeptien, U. (2013). Revisiting “nutrient trapping” in global coupled biogeochemical
659 ocean circulation models. *Global Biogeochemical Cycles*, 27(2), 265–284. doi:10.1002/gbc.20029

660 Dufour, C. O., Griffies, S. M., de Souza, G. F., Frenger, I., Morrison, A. K., Palter, J. B., ... Slater,
661 R. D. (2015). Role of Mesoscale Eddies in Cross-Frontal Transport of Heat and Biogeochemical
662 Tracers in the Southern Ocean. *Journal of Physical Oceanography*, 45(12), 3057–3081.
663 doi:10.1175/jpo-d-14-0240.1

664 Duteil, O., & Oschlies, A. (2011). Sensitivity of simulated extent and future evolution of marine
665 suboxia to mixing intensity. *Geophysical Research Letters*, 38(6), n/a–n/a.
666 doi:10.1029/2011gl046877

667 Duteil, O., Koeve, W., Oschlies, A., Aumont, O., Bianchi, D., Bopp, L., ... Segschneider, J. (2012).
668 Preformed and regenerated phosphate in ocean general circulation models: can right total
669 concentrations be wrong? *Biogeosciences*, 9(5), 1797–1807. doi:10.5194/bg-9-1797-2012

670 Duteil, O., Böning, C. W., & Oschlies, A. (2014). Variability in subtropical-tropical cells drives
671 oxygen levels in the tropical Pacific Ocean. *Geophysical Research Letters*, 41(24), 8926–8934.
672 doi:10.1002/2014gl061774

673 Duteil, O., Oschlies, A., & Böning, C. W. (2018). Pacific Decadal Oscillation and recent oxygen
674 decline in the eastern tropical Pacific Ocean. *Biogeosciences*, 15(23), 7111–7126. doi:10.5194/bg-
675 15-7111-2018

676 Duteil, O. (2019). Wind Synoptic Activity Increases Oxygen Levels in the Tropical Pacific Ocean.
677 *Geophysical Research Letters*, 46(5), 2715–2725. doi:10.1029/2018gl081041

678 Eden, C., & Dengler, M. (2008). Stacked jets in the deep equatorial Atlantic Ocean. *Journal of*
679 *Geophysical Research*, 113(C4). doi:10.1029/2007jc004298

680 Emery, W. J. 2003. Water types and water masses. In: *Encyclopedia of Atmospheric Sciences*.
681 2nd ed. (eds. J.R. Holton, J.A. Curry and J.A. Pyle). Elsevier, Atlanta, GA, pp. 1556–1567

682 Firing, E., Wijffels, S. E., & Hacker, P. (1998). Equatorial subthermocline currents across the
683 Pacific. *Journal of Geophysical Research: Oceans*, 103(C10), 21413–21423.
684 doi:10.1029/98jc01944

685 Firing, E. (1987). Deep zonal currents in the central equatorial Pacific. *Journal of Marine Research*,
686 45(4), 791–812. doi:10.1357/002224087788327163

687 Frenger, I., Bianchi, D., Stührenberg, C., Oschlies, A., Dunne, J., Deutsch, C., ... Schütte, F.
688 (2018). Biogeochemical Role of Subsurface Coherent Eddies in the Ocean: Tracer Cannonballs,
689 Hypoxic Storms, and Microbial Stewpots? *Global Biogeochemical Cycles*, 32(2), 226–249.
690 doi:10.1002/2017gb005743

691 Galbraith, E. D., Dunne, J. P., Gnanadesikan, A., Slater, R. D., Sarmiento, J. L., Dufour, C. O., ...
692 Marvasti, S. S. (2015). Complex functionality with minimal computation: Promise and pitfalls of
693 reduced-tracer ocean biogeochemistry models. *Journal of Advances in Modeling Earth Systems*,
694 7(4), 2012–2028. doi:10.1002/2015ms000463

695 Getzlaff, J., & Dietze, H. (2013). Effects of increased isopycnal diffusivity mimicking the unresolved
696 equatorial intermediate current system in an earth system climate model. *Geophysical Research*
697 *Letters*, 40(10), 2166–2170. doi:10.1002/grl.50419

698 Gnanadesikan, A., Bianchi, D., & Pradal, M. (2013). Critical role for mesoscale eddy diffusion in
699 supplying oxygen to hypoxic ocean waters. *Geophysical Research Letters*, 40(19), 5194–5198.
700 doi:10.1002/grl.50998

701 Gouriou, Y., Delcroix, T., & Eldin, G. (2006). Upper and intermediate circulation in the western
702 equatorial Pacific Ocean in October 1999 and April 2000. *Geophysical Research Letters*, 33(10), n/
703 a–n/a. doi:10.1029/2006gl025941

704 Griffies, S. M., Winton, M., Anderson, W. G., Benson, R., Delworth, T. L., Dufour, C. O., ... Zhang,
705 R. (2015). Impacts on Ocean Heat from Transient Mesoscale Eddies in a Hierarchy of Climate
706 Models. *Journal of Climate*, 28(3), 952–977. doi:10.1175/jcli-d-14-00353.1

707 Haarsma, R. J., Roberts, M. J., Vidale, P. L., Senior, C. A., Bellucci, A., Bao, Q., Chang, P., Corti,
708 S., Fučkar, N. S., Guemas, V., von Hardenberg, J., Hazeleger, W., Kodama, C., Koenigk, T.,
709 Leung, L. R., Lu, J., Luo, J.-J., Mao, J., Mizielinski, M. S., Mizuta, R., Nobre, P., Satoh, M.,
710 Scoccimarro, E., Semmler, T., Small, J., and von Storch, J.-S.(2016). High Resolution Model
711 Intercomparison Project (HighResMIPv1.0)forCMIP6, *Geosci. Model Dev.*, 9, 4185–4208,
712 <https://doi.org/10.5194/gmd-9-4185-2016>

713 Iudicone, D., Rodgers, K. B., Schopp, R., & Madec, G. (2007). An Exchange Window for the
714 Injection of Antarctic Intermediate Water into the South Pacific. *Journal of Physical Oceanography*,
715 37(1), 31–49. doi:10.1175/jpo2985.1

716 Izumo, T. (2005). The equatorial undercurrent, meridional overturning circulation, and their roles in
717 mass and heat exchanges during El Niño events in the tropical Pacific ocean. *Ocean Dynamics*,
718 55(2), 110–123. doi:10.1007/s10236-005-0115-1

719 Khatiwala, S., Tanhua, T., Mikaloff Fletcher, S., Gerber, M., Doney, S. C., Graven, H. D., ...
720 Sabine, C. L. (2013). Global ocean storage of anthropogenic carbon. *Biogeosciences*, 10(4),
721 2169–2191. doi:10.5194/bg-10-2169-2013

722 Kawabe, M., & Fujio, S. (2010). Pacific ocean circulation based on observation. *Journal of*
723 *Oceanography*, 66(3), 389–403. doi:10.1007/s10872-010-0034-8

724 Keller, D. P., Oschlies, A., & Eby, M. (2012). A new marine ecosystem model for the University of
725 Victoria Earth System Climate Model. *Geoscientific Model Development*, 5(5), 1195–1220.
726 doi:10.5194/gmd-5-1195-2012

727 Koshlyakov, M.N. and Tarakanov, R.Y. (2003). Antarctic Bottom Water in the Pacific sector of the
728 Southern Ocean, *Oceanology* 43(1):1-15

729 Kriest, I., Khatiwala, S., & Oschlies, A. (2010). Towards an assessment of simple global marine
730 biogeochemical models of different complexity. *Progress in Oceanography*, 86(3-4), 337–360.
731 doi:10.1016/j.pocean.2010.05.002

732 Kwiatkowski, L., Torres, O., Bopp, L., Aumont, O., Chamberlain, M., Christian, J. R., Dunne, J. P.,
733 Gehlen, M., Ilyina, T., John, J. G., Lenton, A., Li, H., Lovenduski, N. S., Orr, J. C., Palmieri, J.,
734 Santana-Falcón, Y., Schwinger, J., Séférian, R., Stock, C. A., Tagliabue, A., Takano, Y., Tjiputra,
735 J., Toyama, K., Tsujino, H., Watanabe, M., Yamamoto, A., Yool, A., and Ziehn, T.: Twenty-first
736 century ocean warming, acidification, deoxygenation, and upper-ocean nutrient and primary
737 production decline from CMIP6 model projections, *Biogeosciences*, 17, 3439–3470, [https://doi.org/](https://doi.org/10.5194/bg-17-3439-2020)
738 10.5194/bg-17-3439-2020, 2020.

739 Lachkar, Z., Orr, J. C., & Dutay, J.-C. (2009). Seasonal and mesoscale variability of oceanic
740 transport of anthropogenic CO₂. *Biogeosciences*, 6(11), 2509–2523. doi:10.5194/bg-6-2509-2009

741 Large, W. G., & Yeager, S. G. (2008). The global climatology of an interannually varying air–sea
742 flux data set. *Climate Dynamics*, 33(2-3), 341–364. doi:10.1007/s00382-008-0441-3

743 Lübbecke, J. F., Böning, C. W., & Biastoch, A. (2008). Variability in the subtropical-tropical cells
744 and its effect on near-surface temperature of the equatorial Pacific: a model study. *Ocean Science*,
745 4(1), 73–88. doi:10.5194/os-4-73-2008

746 Madec, G., Bourdallé-Badie, R., Pierre-Antoine Bouttier, Bricaud, C., Bruciaferri, D., Calvert, D.,
747 Chanut, J., Clementi, E., Coward, A., Delrosso, D., Ethé, C., Flavoni, S., Graham, T., Harle, J.,
748 Iovino, D., Lea, D., Lévy, C., Lovato, T., Martin, N., ... Vancoppenolle, M. (2017). NEMO ocean
749 engine. <https://doi.org/10.5281/ZENODO.3248739> Marin, F., Kestenare, E., Delcroix, T., Durand,
750 F., Cravatte, S., Eldin, G., & Bourdallé-Badie, R. (2010). Annual Reversal of the Equatorial
751 Intermediate Current in the Pacific: Observations and Model Diagnostics. *Journal of Physical*
752 *Oceanography*, 40(5), 915–933. doi:10.1175/2009jpo4318.1

753 Martin, J. H., Knauer, G. A., Karl, D. M., & Broenkow, W. W. (1987). VERTEX: carbon cycling in
754 the northeast Pacific. *Deep Sea Research Part A. Oceanographic Research Papers*, 34(2), 267–
755 285. doi:10.1016/0198-0149(87)90086-0

756 Meijers, A. J. S. (2014). The Southern Ocean in the Coupled Model Intercomparison Project phase
757 5. *Philosophical Transactions of the Royal Society A: Mathematical, Physical and Engineering*
758 *Sciences*, 372(2019), 20130296. doi:10.1098/rsta.2013.0296

759 Ménesguen, C., Delpech, A., Marin, F., Cravatte, S., Schopp, R., & Morel, Y. (2019). Observations
760 and Mechanisms for the Formation of Deep Equatorial and Tropical Circulation. *Earth and Space*
761 *Science*, 6(3), 370–386. doi:10.1029/2018ea000438

762 Molinelli EJ (1981) The Antarctic influence on Antarctic Intermediate Water. *J Mar Res* 39:267–293

763 Oschlies, A., Brandt, P., Stramma, L., & Schmidtko, S. (2018). Drivers and mechanisms of ocean
764 deoxygenation. *Nature Geoscience*, 11(7), 467–473. doi:10.1038/s41561-018-0152-2

765 Palter, J. B., Sarmiento, J. L., Gnanadesikan, A., Simeon, J., and Slater, R. D. (2010). Fueling
766 export production: nutrient return pathways from the deep ocean and their dependence on the
767 Meridional Overturning Circulation, *Biogeosciences*, 7, 3549–3568, doi:10.5194/bg-7-3549-2010

768 Panassa, E., Santana-Casiano, J. M., González-Dávila, M., Hoppema, M., van Heuven, S. M. A. .,
769 Völker, C., ... Hauck, J. (2018). Variability of nutrients and carbon dioxide in the Antarctic
770 Intermediate Water between 1990 and 2014. *Ocean Dynamics*, 68(3), 295–308.
771 doi:10.1007/s10236-018-1131-2

772 Pardo, P. C., Pérez, F. F., Velo, A., & Gilcoto, M. (2012). Water masses distribution in the
773 Southern Ocean: Improvement of an extended OMP (eOMP) analysis. *Progress in Oceanography*,
774 103, 92–105. doi:10.1016/j.pocean.2012.06.002

775 Paulmier, A., Ruiz-Pino (2009), D. Oxygen minimum zones (OMZs) in the modern ocean, *Progress*
776 *in Oceanography*, 80(3), 113-128, doi:10.1016/j.pocean.2008.08.001.

777 Qu, T., & Lindstrom, E. J. (2004). Northward Intrusion of Antarctic Intermediate Water in the
778 Western Pacific*. *Journal of Physical Oceanography*, 34(9), 2104–2118. doi:10.1175/1520-
779 0485(2004)034<2104:nioaiw>2.0.co;2

780 Resplandy, L., Bopp, L., Orr, J. C., & Dunne, J. P. (2013). Role of mode and intermediate waters in
781 future ocean acidification: Analysis of CMIP5 models. *Geophysical Research Letters*, 40(12),
782 3091–3095. doi:10.1002/grl.50414

783 Rowe, G. D., Firing, E., & Johnson, G. C. (2000). Pacific Equatorial Subsurface Countercurrent
784 Velocity, Transport, and Potential Vorticity*. *Journal of Physical Oceanography*, 30(6), 1172–1187.
785 doi:10.1175/1520-0485(2000)030<1172:pescvt>2.0.co;2

786 Russell, J. L., & Dickson, A. G. (2003). Variability in oxygen and nutrients in South Pacific Antarctic
787 Intermediate Water. *Global Biogeochemical Cycles*, 17(2), n/a–n/a. doi:10.1029/2000gb001317

788 Sabine, C. L. (2004). The Oceanic Sink for Anthropogenic CO₂. *Science*, 305(5682), 367–371.
789 doi:10.1126/science.1097403

790 Sallée, J.-B., Shuckburgh, E., Bruneau, N., Meijers, A. J. S., Bracegirdle, T. J., Wang, Z., & Roy, T.
791 (2013). Assessment of Southern Ocean water mass circulation and characteristics in CMIP5
792 models: Historical bias and forcing response. *Journal of Geophysical Research: Oceans*, 118(4),
793 1830–1844. doi:10.1002/jgrc.20135

794 Schmidtko, S., Stramma, L., & Visbeck, M. (2017). Decline in global oceanic oxygen content during
795 the past five decades. *Nature*, 542(7641), 335–339. doi:10.1038/nature21399

796 Sen Gupta, A., & England, M. H. (2007). Evaluation of Interior Circulation in a High-Resolution
797 Global Ocean Model. Part II: Southern Hemisphere Intermediate, Mode, and Thermocline Waters.
798 *Journal of Physical Oceanography*, 37(11), 2612–2636. doi:10.1175/2007jpo3644.1

799 Shigemitsu, M., Yamamoto, A., Oka, A., & Yamanaka, Y. (2017). One possible uncertainty in
800 CMIP5 projections of low-oxygen water volume in the Eastern Tropical Pacific. *Global*
801 *Biogeochemical Cycles*, 31(5), 804–820. doi:10.1002/2016gb005447

802 Sloyan, B. M., & Kamenkovich, I. V. (2007). Simulation of Subantarctic Mode and Antarctic
803 Intermediate Waters in Climate Models. *Journal of Climate*, 20(20), 5061–5080.
804 doi:10.1175/jcli4295.1

805 Sloyan, B. M., & Rintoul, S. R. (2001). Circulation, Renewal, and Modification of Antarctic Mode
806 and Intermediate Water*. *Journal of Physical Oceanography*, 31(4), 1005–1030. doi:10.1175/1520-
807 0485(2001)031<1005:cramoa>2.0.co;2

808 Takano, Y., Ito, T., & Deutsch, C. (2018). Projected Centennial Oxygen Trends and Their
809 Attribution to Distinct Ocean Climate Forcings. *Global Biogeochemical Cycles*, 32(9), 1329–1349.
810 doi:10.1029/2018gb005939

811 Talley, L. D. (1993). Distribution and Formation of North Pacific Intermediate Water. *Journal of*
812 *Physical Oceanography*, 23(3), 517–537. doi:10.1175/1520-0485(1993)023<0517:dafonp>2.0.co;2

813 Weaver, A. J., Eby, M., Wiebe, E. C., Bitz, C. M., Duffy, P. B., Ewen, T. L., ... Yoshimori, M.
814 (2001). The UVic earth system climate model: Model description, climatology, and applications to
815 past, present and future climates. *Atmosphere-Ocean*, 39(4), 361–428.
816 doi:10.1080/07055900.2001.9649686

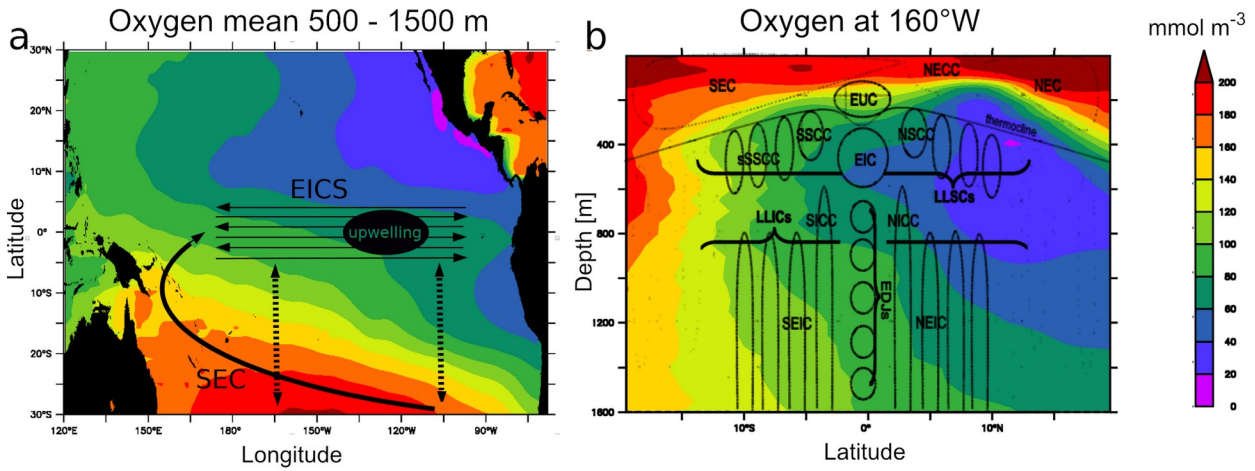
817 Xu, L., Li, P., Xie, S. et al. (2016). Observing mesoscale eddy effects on mode-water subduction
818 and transport in the North Pacific. *Nature Communications*, 10505 (2016),
819 doi.org/10.1038/ncomms10505

820 Zenk, W., Siedler, G., Ishida, A., Holfort, J., Kashino, Y., Kuroda, Y., ... Müller, T. J. (2005).
821 Pathways and variability of the Antarctic Intermediate Water in the western equatorial Pacific
822 Ocean. *Progress in Oceanography*, 67(1-2), 245–281. doi:10.1016/j.pocean.2005.05.003

823 Zhu, C., Liu, Z., & Gu, S. (2017). Model bias for South Atlantic Antarctic intermediate water in
824 CMIP5. *Climate Dynamics*, 50(9-10), 3613–3624. doi:10.1007/s00382-017-3828-1

825
826
827
828
829
830
831
832
833
834
835
836
837
838
839
840
841

842 **Figures and Table**



843

844

845 Figure 1 : a- schema summarizing the intermediate water masses (IWM) pathway from the
 846 subtropics into the equatorial regions. EICS : Equatorial Intermediate Current System. SEC : South
 847 Equatorial Current. Dashed line : isopycnal diffusive processes. Observed (World Ocean Atlas)
 848 oxygen levels ($\text{mmol}\cdot\text{m}^{-3}$) in the lower thermocline (mean 500-1500m) are represented in color. b -
 849 schema (adapted from Menesguen et al., 2019) illustrating the complexity of the EICS, extending
 850 below the thermocline till more than 2000 m depth (see section 4.1 for a detailed description).
 851 Observed (World Ocean Atlas) oxygen levels at 160°W are represented in color. SEC : South
 852 Equatorial Current. N/SEC : North/South Equatorial Current. NECC: North Equatorial Counter
 853 Current. EUC : Equatorial Undercurrent. EIC : Equatorial Intermediate Current. N/SSCC : North /
 854 South Subsurface Counter Current. LLSC : Low Latitude Subsurface Currents. LLIC : Low
 855 Latitudes Intermediate Currents. N/SEIC : North / South Equatorial Intermediate Current. N/SICC :
 856 North / South Intermediate Current. EDJ : Equatorial Deep Jets.

857

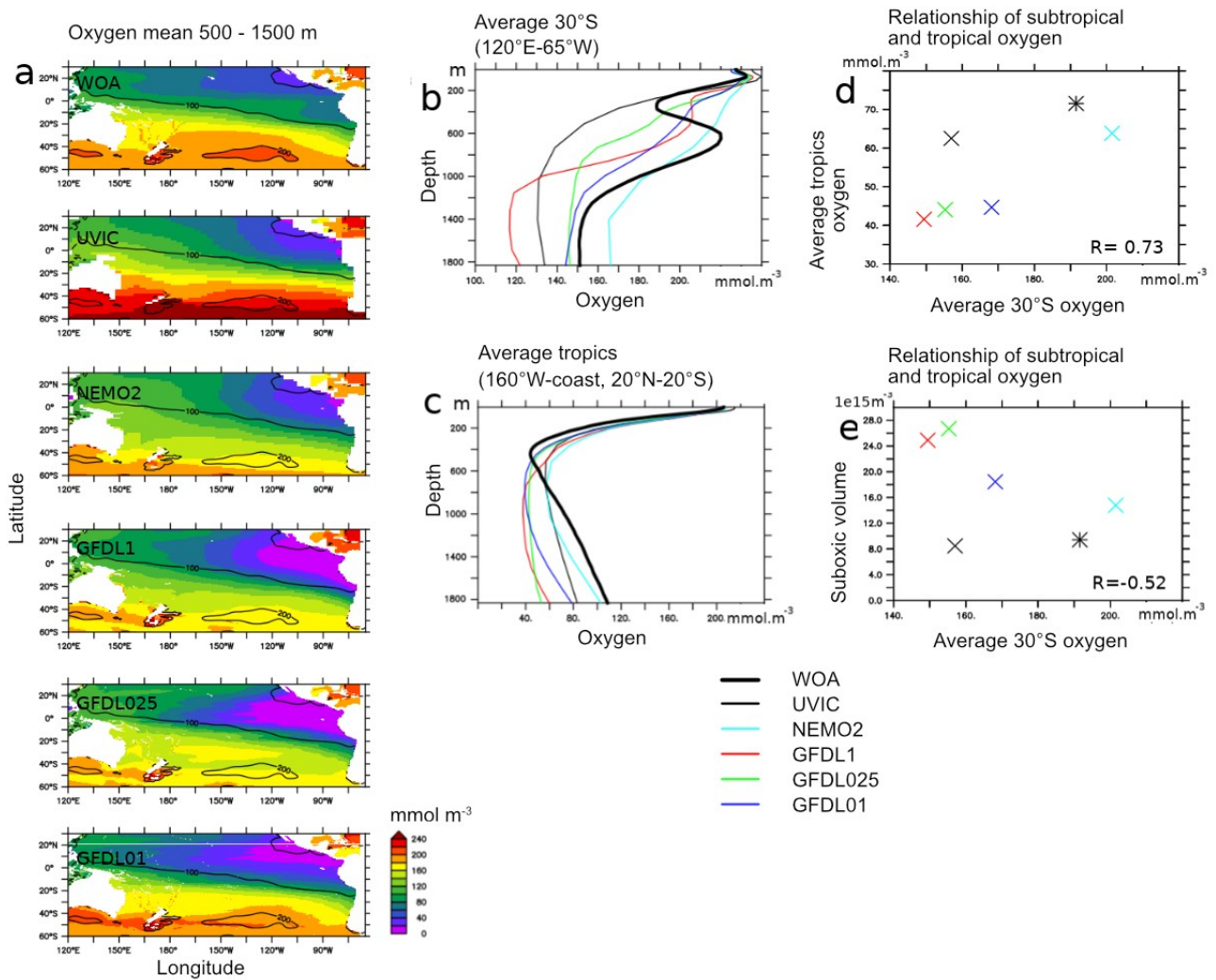
858

859

860

861

862



863

864

865

866

867

868

869

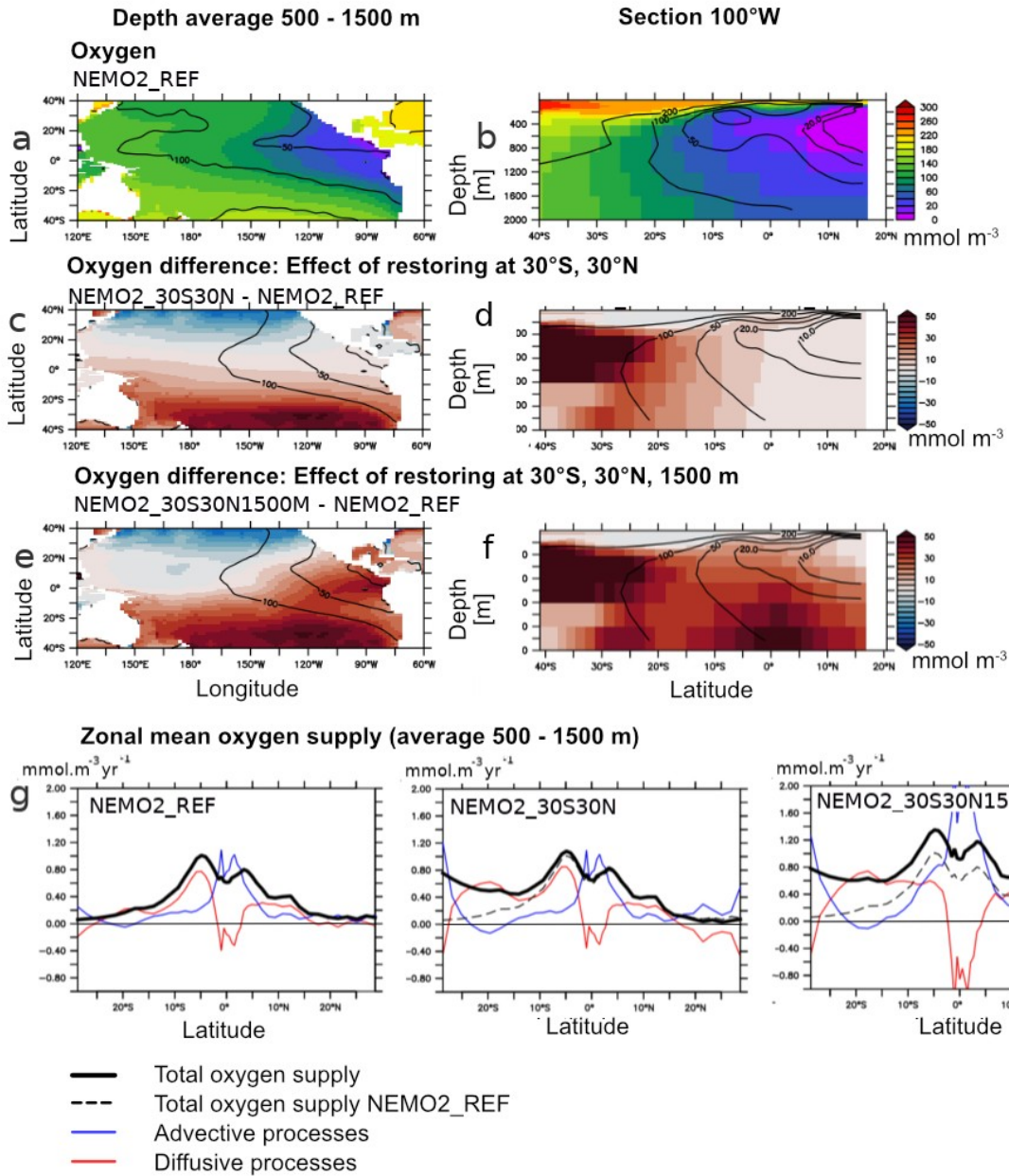
870

871

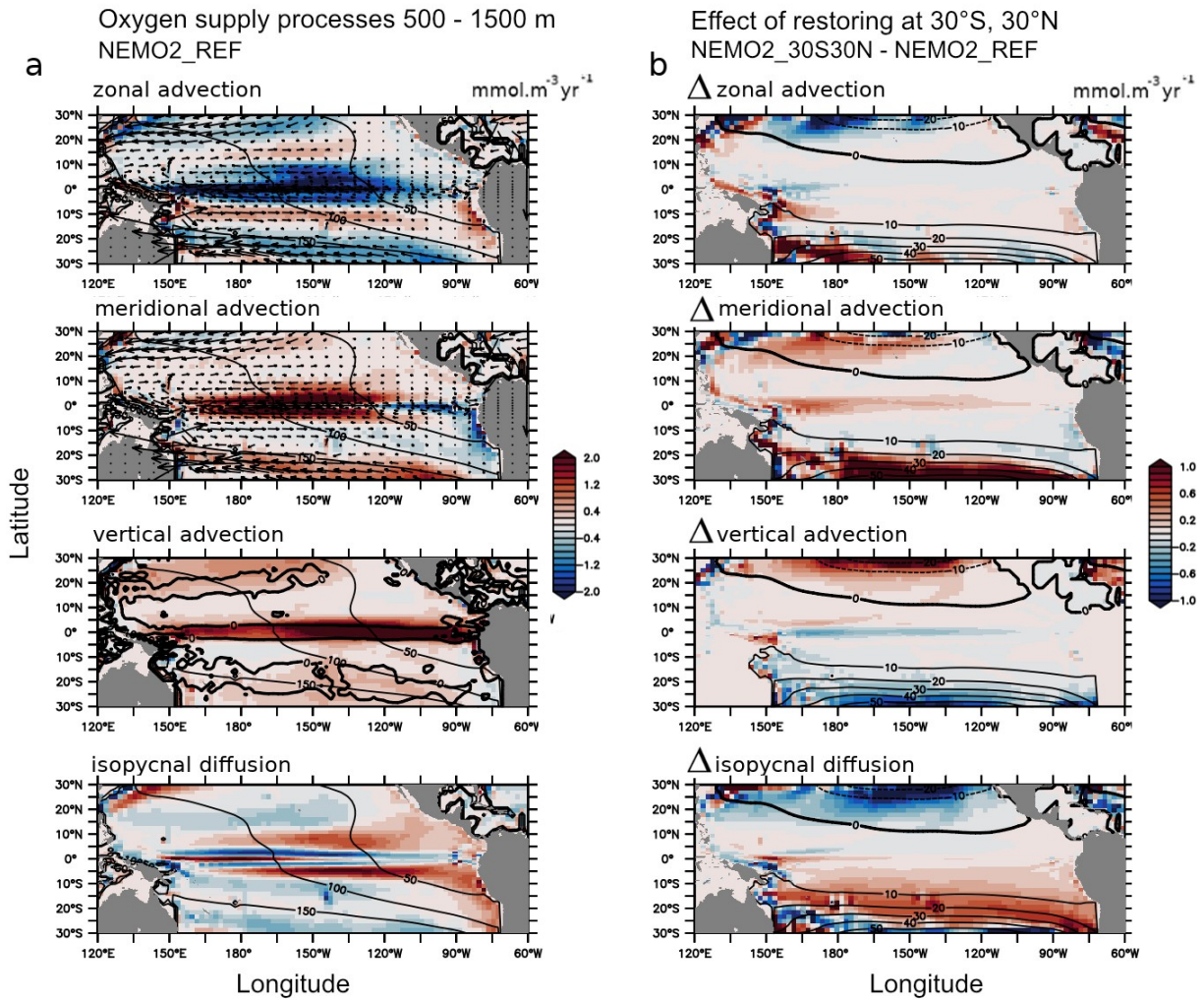
872

873

874 Figure 2 : a- oxygen levels (mmol.m⁻³) in observations (World Ocean Atlas - WOA) (mean 500 –
 875 1500 m) and models (UVIC, NEMO2, GFDL1, GFDL025, GFDL01). Contours correspond to WOA
 876 values. b: average “30°S” (120°E-65°W, 30°S) c : average “tropics” (160°W-coast, 20°N-20°S). d:
 877 average “30°S” vs “tropics”. e: average “30°S” vs volume of tropical suboxic ocean (oxygen lower
 878 than 20 mmol.m⁻³) regions (1e15m³). b-e : UVIC : black, NEMO2 : cyan, GFDL1 : red, GFDL025,
 879 green; GFDL01 : blue, WOA: bold line (b,c) and star (d,e).



881 Figure 3 : a,b: Oxygen (mmol.m⁻³) in the experiments NEMO2_REF (color) and World Ocean Atlas
 882 (contour) (a- average 500-1500 m, b- 100°W). c,d: Oxygen (mmol.m⁻³) difference (c- average 500 –
 883 1500m, d- 100°W) between the experiments NEMO2_30S30N minus NEMO2_REF. e,f : Oxygen
 884 (mmol.m⁻³) difference (e- average 500-1500m, f- 100°W) between the experiments
 885 NEMO2_30S30N1500M minus NEMO2_REF. g- basin zonal average (average 500 - 1500 m) of
 886 the oxygen total supply (bold) (mmol.m⁻³.year⁻¹), advective processes (blue) and isopycnal diffusion
 887 (red) in NEMO2_REF, NEMO2_30S30N, NEMO2_30S30N1500M. The dashed line is the oxygen
 888 total supply in NEMO2_REF.
 889



891 Figure 4 : a- Oxygen supply processes (mmol.m⁻³.year⁻¹ – average 500 - 1500m) in NEMO2_REF :
 892 zonal advection, meridional advection, vertical advection, isopycnal diffusion. The mean meridional
 893 and zonal currents are displayed as vectors (meridional, zonal advection). The mean vertical
 894 current (0 isoline) is represented as bold contour (vertical advection). Oxygen levels (mmol.m⁻³)
 895 are displayed in black contour. b- Difference in oxygen supply processes (mmol.m⁻³.year⁻¹ –
 896 average 500-1500m) between NEMO2_30S30N and NEMO2_REF : zonal advection, meridional
 897 advection, vertical advection, isopycnal diffusion. The NEMO2_30S30N – NEMO2_REF oxygen
 898 anomaly (mmol.m⁻³) is displayed in contour.

899

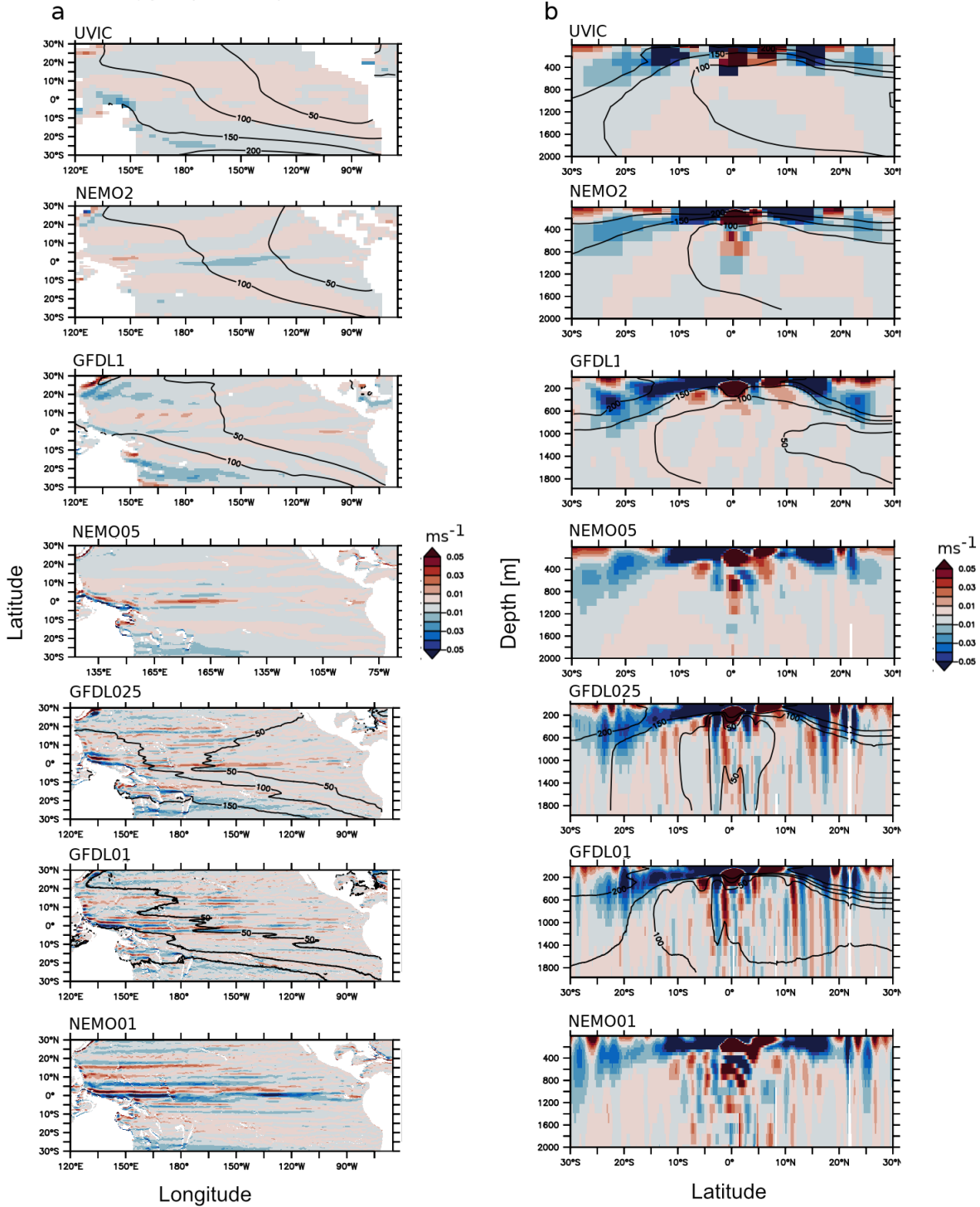
900

901

902

Zonal velocity component at 1000 m (colors) and oxygen (contours)

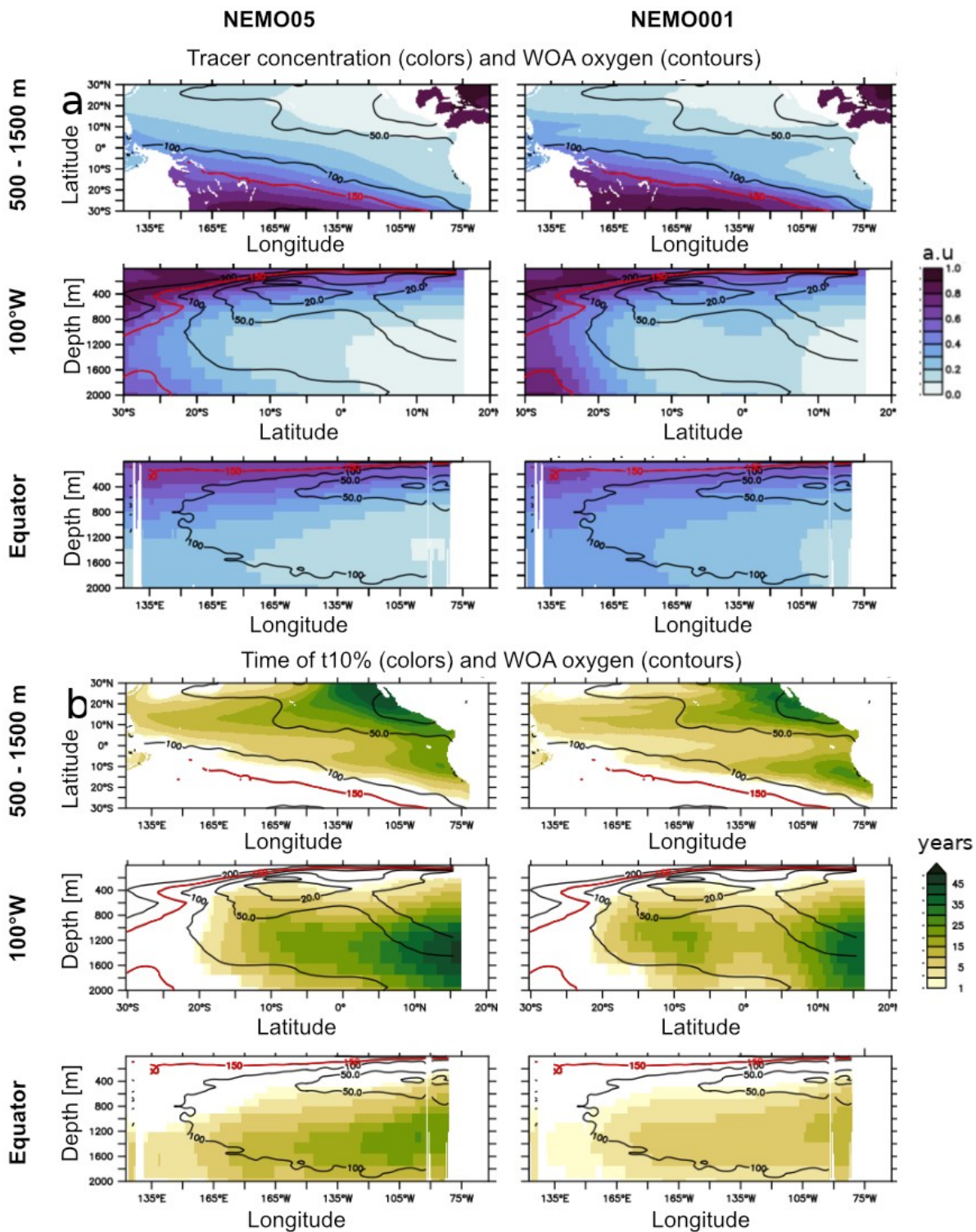
Zonal velocity component at 100°W (colors) and oxygen (contours)



903

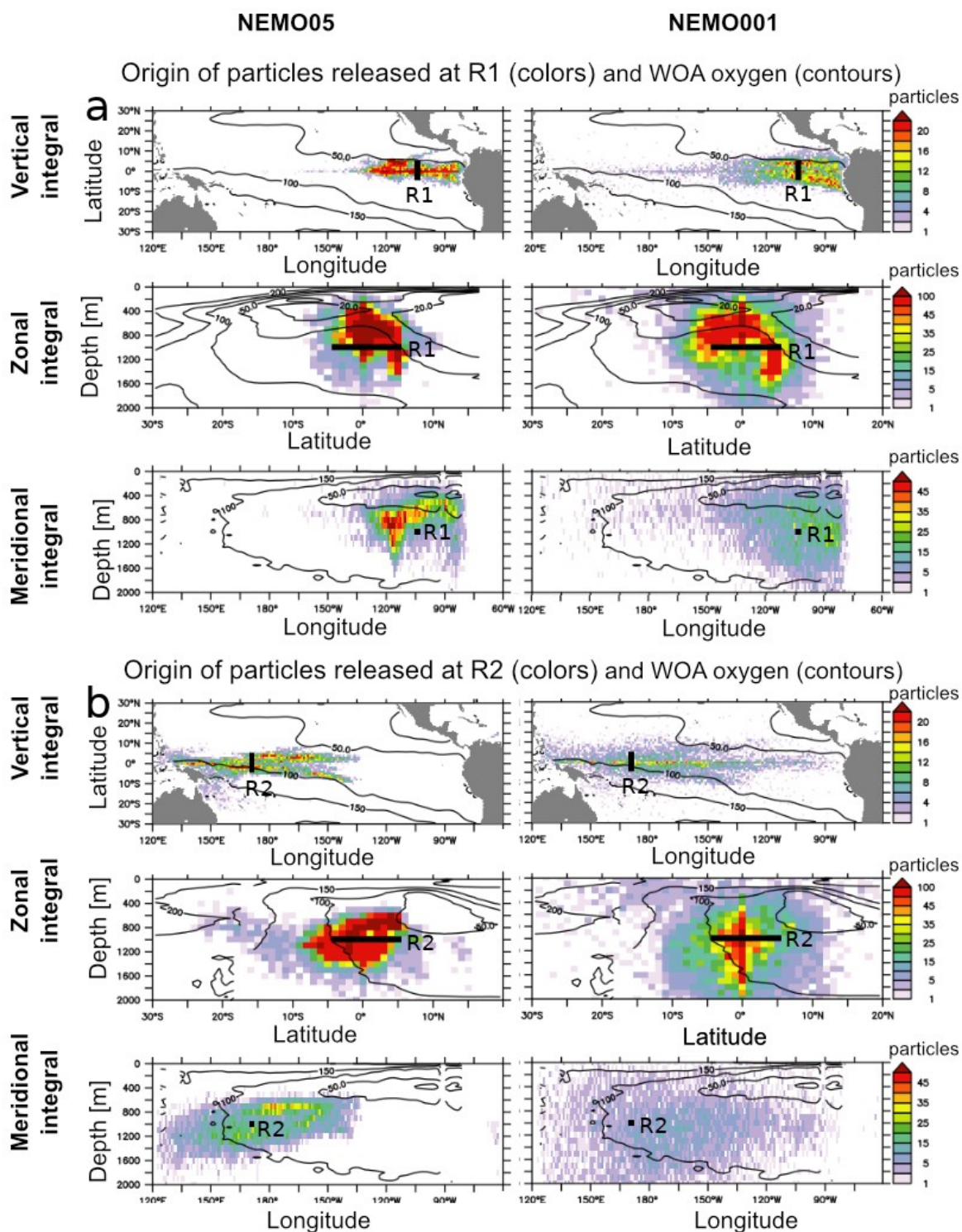
904 Figure 5 : mean currents velocity (ms^{-1}) at a- 1000 m depth b- 100°W in UVIC, NEMO2, NEMO05,
 905 GFDL025, GFDL01, NEMO01. The mean oxygen levels (mmol.m^{-3}) (when coupled circulation-
 906 biogeochemical experiments have been performed – see Table 1) are displayed in contour.

907

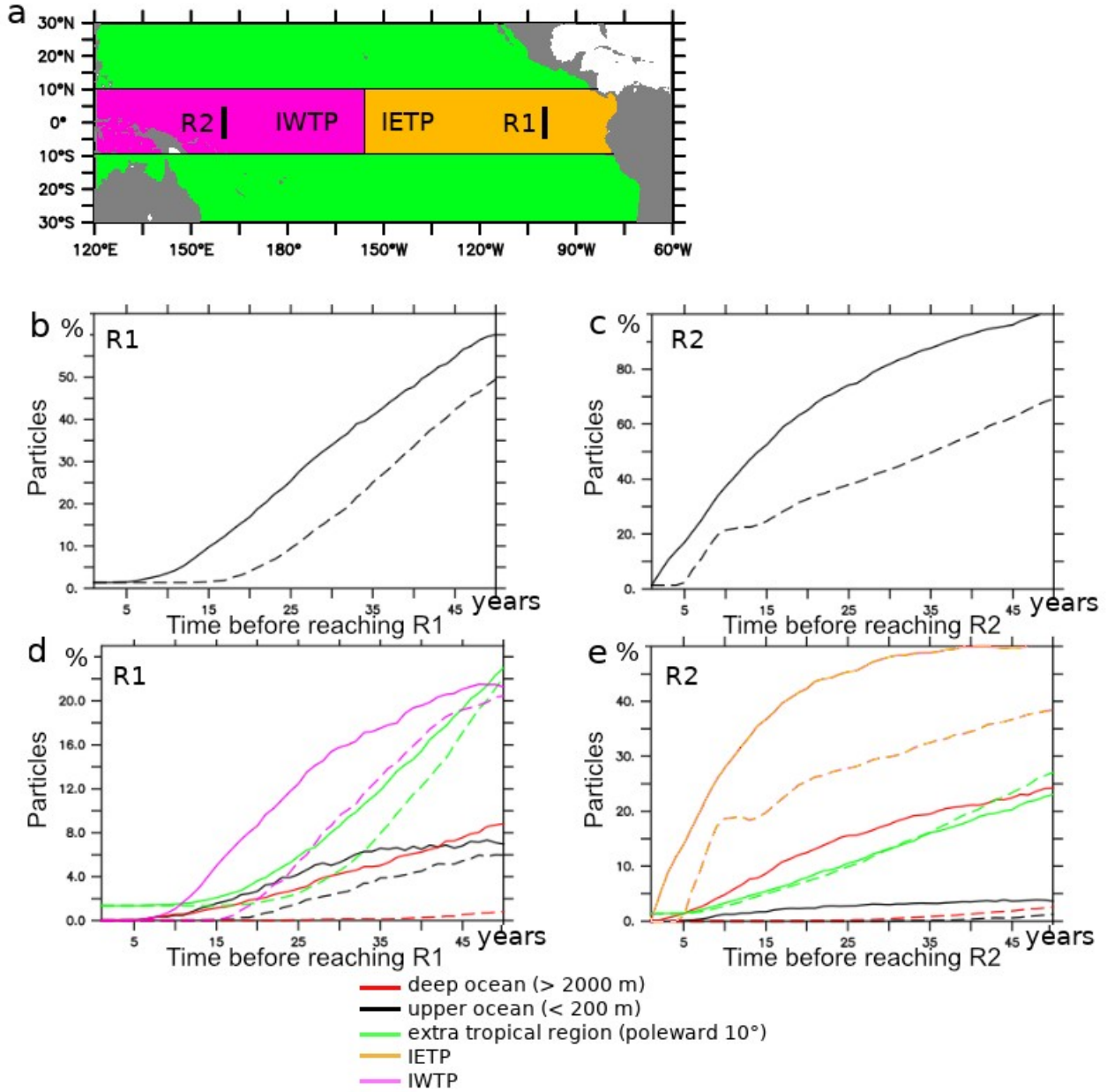


908

909 Figure 6: a : tracer concentration (arbitrary unit) after 60 years integration in NEMO05 and
 910 NEMO01: average 500-1500m, section 100°W, equatorial section. b: Time (years) at which the
 911 released tracer reaches the concentration 0.1 (t10%) in NEMO05 and NEMO01: average 500-
 912 1500m, section 100°W, equatorial section. In all the subpanels, the WOA oxygen levels are
 913 displayed in contour. The red contour is the WOA 150 mmol.m⁻³ oxygen isoline, used to initialize
 914 the tracer level.



915
 916 Figure 7 : Density (number of particles in a 1°x1°x100m depth box) distribution of the location of
 917 released Lagrangian particles (15 years backward integration starting from the final experiment
 918 state) in NEMO05 and NEMO01. The release location is identified in bold and is located a- at
 919 100°W/5°N-5S/1000 m depth (R1). b- at 160°E/5°N-5°S/1000 m depth (R2). The particles have
 920 been integrated vertically, zonally and meridionally. The observed mean oxygen levels (WOA) are
 921 displayed in contour.



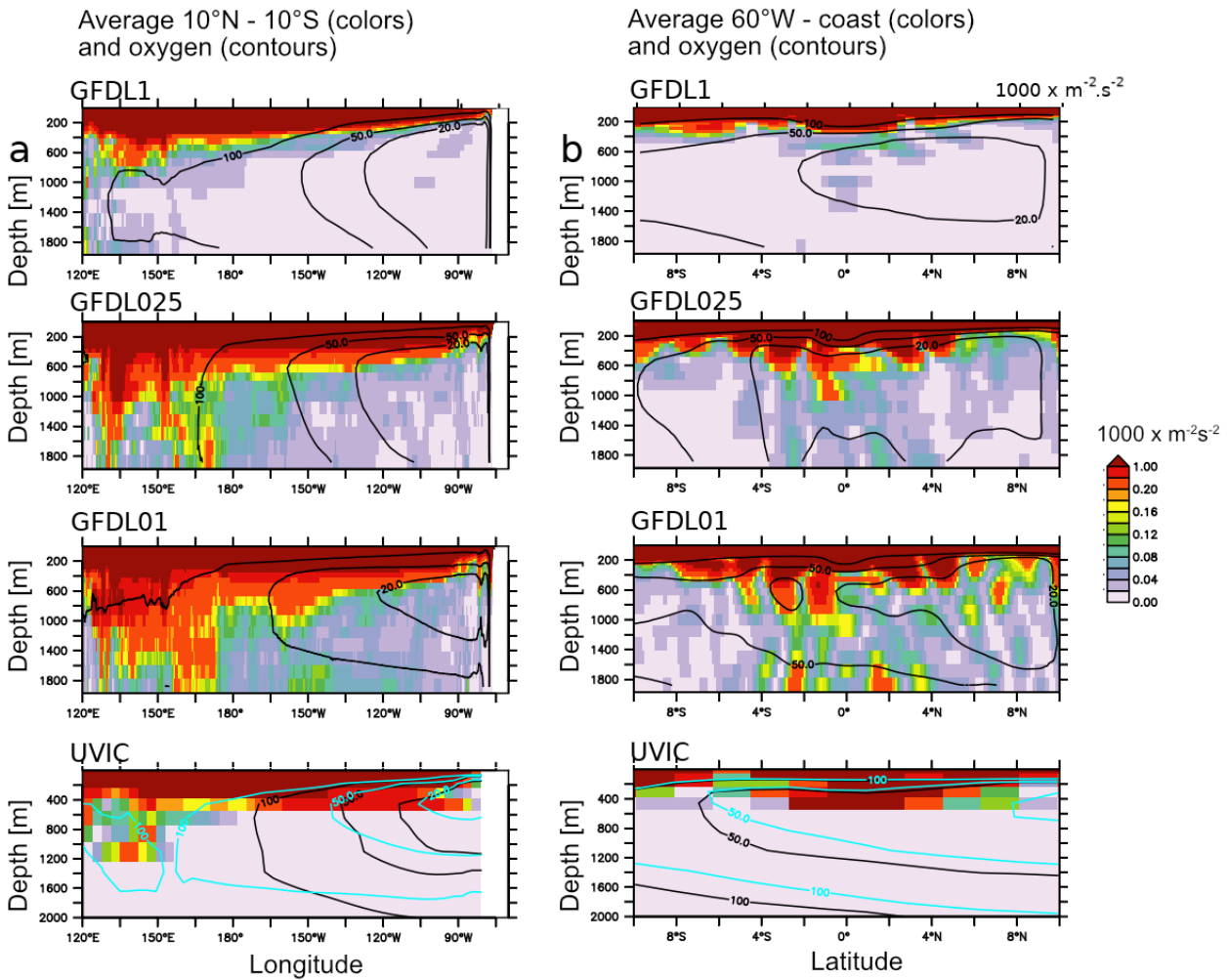
923

924

925 Figure 8 : a- schema summarizing the releases (R1: 100°W / 5°N-5°S / 1000 m , R2: 160°E /
 926 5°N-5°S / 1000 m) location, the IETP (Intermediate Eastern Tropical Pacific), IWTP (Intermediate
 927 Western Tropical Pacific) regional extension. b. percentage of particles (release R1) originating
 928 from outside the IETP ocean region. b- percentage of particles (release R2) originating from
 929 outside the IWTP ocean region. d- percentage of particles (release R1) originating from the upper
 930 ocean (shallower than 200 m), the deeper ocean (deeper than 2000 m), subtropical regions
 931 (poleward 10°), the IWTP. e- percentage of particles (release R2) originating from the upper ocean
 932 (shallower than 200 m), the deeper ocean (deeper than 2000 m), subtropical regions (poleward
 933 10°), the IETP.

934

Mean kinetic energy



936

937

938 Figure 9 : a - Mean Kinetic Energy ($m^2.s^{-2} \times 1000$) (average $10^\circ N-10^\circ S$) in GFDL01, GFDL025,
 939 GFDL01, UVIC, b - similar to a. but average $160^\circ W$ - coast. Oxygen levels ($mmol.m^{-3}$) are displayed
 940 in black contour. The blue contour corresponds to UVIC GD13 (Getzlaff and Dietze, 2013,
 941 including an anisotropic increase of lateral diffusion at the equator)

942

943

944

945

946

947

948

949

950

951 Table 1 :

Model	Resolution	Atmosphere	Integration (years)	BGC	Model Reference (circulation)	Model Reference (BGC)
Mean state comparison						
UVIC	2.8°	Coupled (temperature, humidity) Forced (NCEP/NCAR wind stress)	10000	UVIC-BGC	Weaver et al., 2001	Keller et al., 2012
NEMO2	2° (0.5 eq)	Forced COREv2 "normal year"	1000	NPZD-O2	Madec et al., 2015	Kriest et al., 2010 Duteil et al., 2014
GFDL1	1°	Coupled	190	BLING	Delworth et al., 2012, Griffies et al., 2015	Galbraith et al., 2015
GFDL025	0.25 °	Coupled	190	BLING		
GFDL01	0.1°	Coupled	190	BLING		
Process oriented experiments						
Model	Resolution	Atmosphere	Integration (years)	BGC	Characteristics	
NEMO2-REF -30N30S -30N30S1500M (section 2.2.1)	2° (0.5 eq)	Forced COREv2 1948-2007	60	NPZD-O2	<ul style="list-style-type: none"> - control experiment - O2 restoring to WOA at 30°N/30°S - O2 restoring to WOA at 30°N/30°S/1500m 	
NEMO05 (section 2.2.2)	0.5°	Forced COREv2 1948 - 2007	60	Tracer release	<ul style="list-style-type: none"> - Tracer initialized to 1 (O2 WOA > 150 mmol.m-3) or 0 (O2 WOA < 150 mmol-m-3) 	
NEMO01 (section 2.2.2)	0.1°	Forced COREv2 1948 – 2007	60	Tracer release		

952

953

954

955

956

957

958

959

960

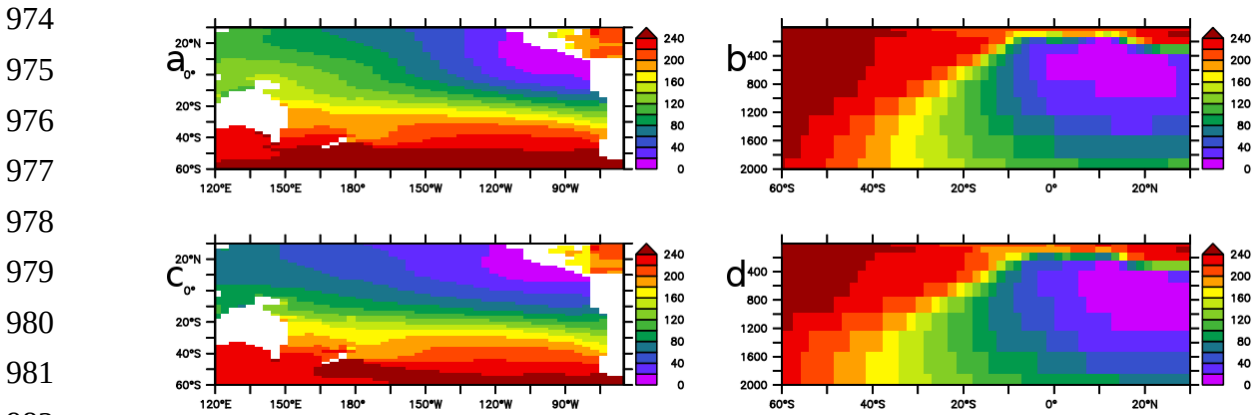
961

962 **Annex A**

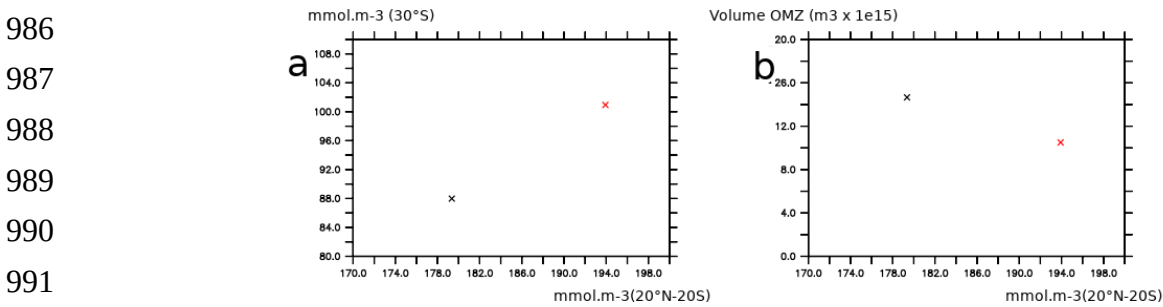
963 The differences in oxygen levels between the “models groups” (GFDL suite, UVIC, NEMO2) are
 964 partly related to differences in the atmospheric fields employed and the integration time (see 2).

965
 966 1. Wind forcing

967 Zonal wind mean stress typically varies by 5 to 20 % between the different wind products
 968 (Chauduri et al., 2013). To test this impact, we performed an experiment using the UVIC model
 969 using 2 different wind products (NCEP and COREv2 – Large and Yeager, 2009) (Figure A1). While
 970 the shape of the OMZ shows slight differences, the volume of the OMZ and the mean oxygen
 971 levels in the tropical regions and in the mid latitudes are similar. Consistent with the Figure 2,
 972 higher oxygen levels at 30°S lead to higher oxygen levels in the tropical ocean and to a smaller
 973 OMZ volume (Figure A2)



983 Figure A1 : Oxygen levels in UVIC (10000 years integration) a- mean 500-1500 m forcing NCEP.
 984 b- section 120°W forcing NCEP. c- mean 500-1500 m forcing COREv2, d- section 120°W forcing
 985 COREv2.

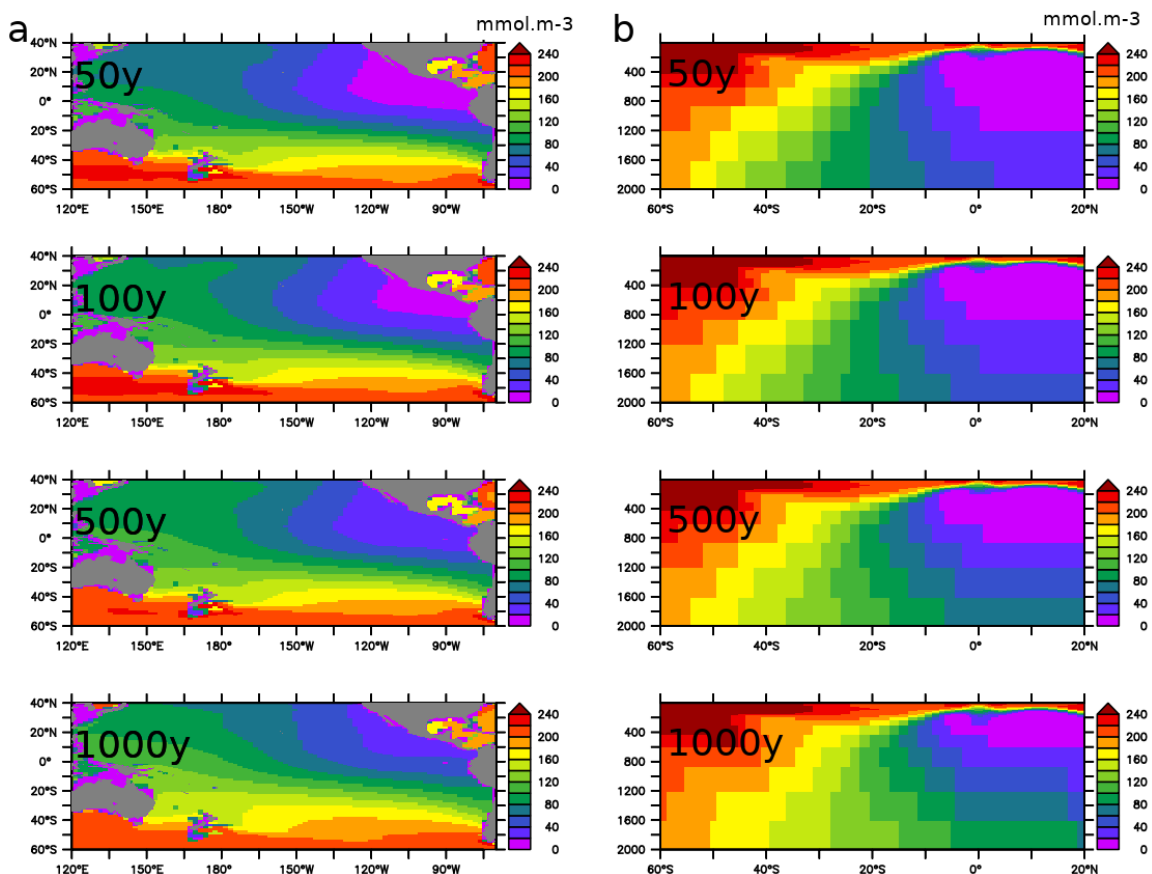


992 Figure A2 : a - Oxygen
 993 levels in UVIC (10000 years integration) at 30°S (zonal mean in the Pacific Ocean from surface to
 994 2000 m depth) and in the tropical regions (20°S-20°N, averaged over the whole Pacific Ocean). b -
 995 Oxygen levels in UVIC (10000 years integration) at 30°S (zonal mean in the Pacific Ocean, from
 996 surface to 2000 m depth) and volume of the OMZ in the Pacific Ocean. The configuration forced by
 997 COREv2 is shown in black, the configuration forced by NCEP is shown in red.

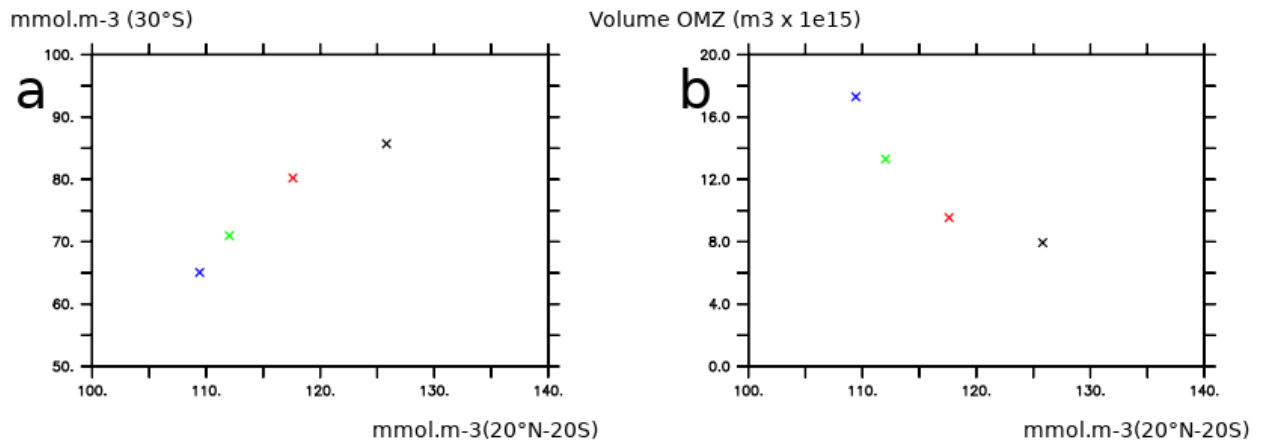
998 2. Spinup state

999 In complement, the spinup state of the model also impacts the oxygen levels as the deep ocean
 1000 needs thousands of years to be in equilibrium. It may explain why UVIC (integrated for 10000
 1001 years) is characterized by much larger oxygen levels than the GFDL model suite (integrated for
 1002 190 years). As an example, the Figure A3 shows the evolution of oxygen levels during spinup in
 1003 NEMO2. Larger oxygen levels at 30°S (e.g after 1000 years of integration) are characterized by a
 1004 smaller OMZ volume (which is consistent with Fig 2) (Figure A4)

1005
 1006

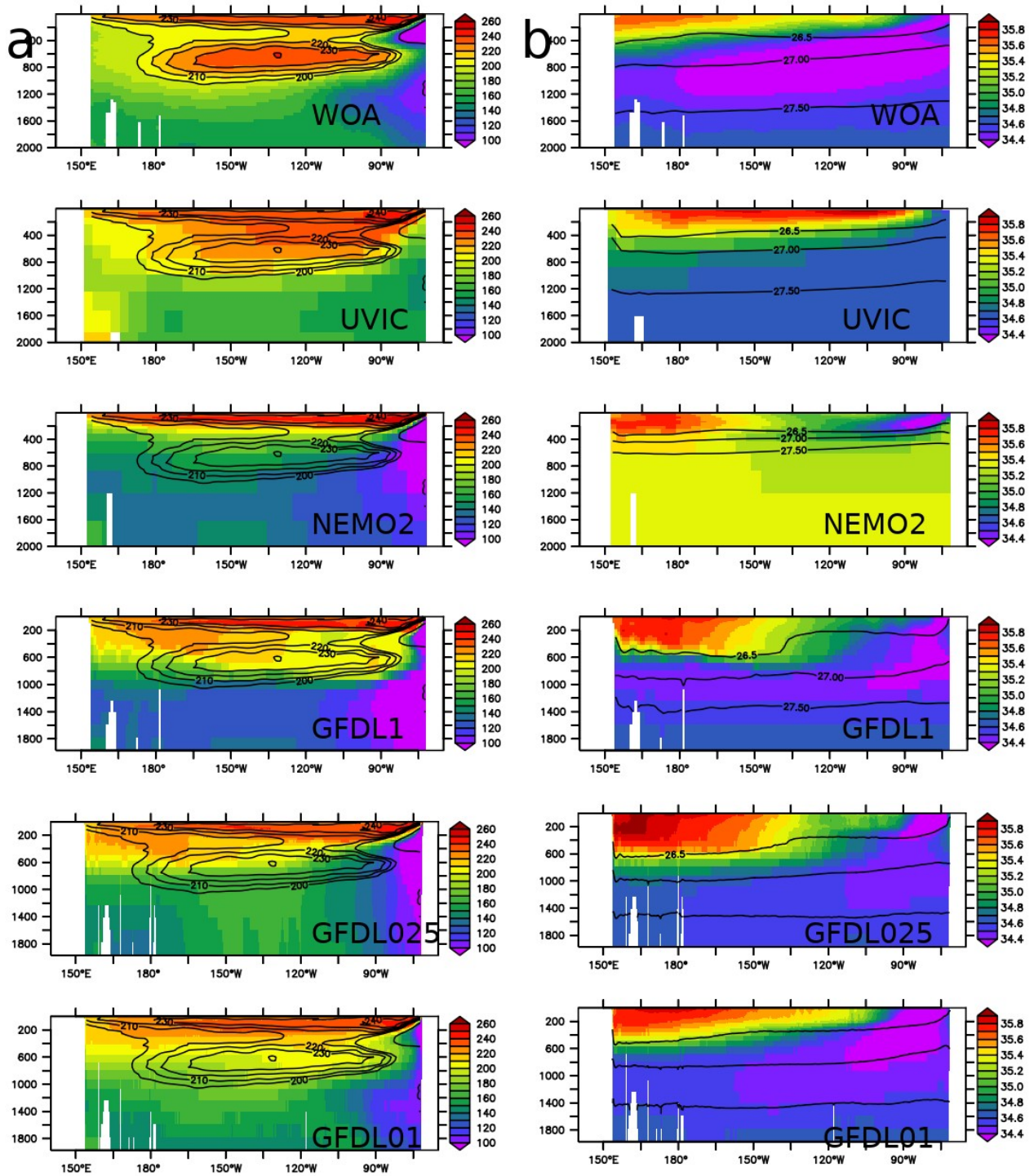


1007 Figure A3 : oxygen levels at a - intermediate depth (average 500 – 2000 m) and b - 120°W in
 1008 NEMO2 after 50, 100,500 and 1000 years integration



1010 Figure A4 : a - Oxygen levels in NEMO2 at 30°S (zonal mean in the Pacific Ocean from surface to
 1011 2000 m depth) and in the tropical regions (20°S-20°N, averaged over the whole Pacific Ocean from
 1012 surface to 2000 m depth). b - Oxygen levels in NEMO2 at 30°S (zonal mean in the Pacific Ocean
 1013 from surface to 2000 m depth) and volume of the OMZ in the Pacific Ocean. The color of the cross
 1014 depends of the integration duration (black : 50 years, red : 100 years, green : 500 years, blue 1000
 1015 years).

1016
 1017
 1018
 1019
 1020
 1021
 1022
 1023
 1024
 1025
 1026
 1027
 1028
 1029
 1030
 1031
 1032
 1033
 1034



1035

1036 Figure A5 : a - oxygen levels (mmol.m-3) in observations and models at 30°S. The WOA oxygen

1037 levels are displayed in contour. b- salinity in observations and models at 30°S. The density

1038 anomaly (26.5, 27, 27.5) is displayed in contour.

1039

1040

1041

1042

1043 References

- 1044 Chaudhuri, Ayan & Ponte, Rui & Forget, Gael & Heimbach, Patrick. (2013). A Comparison of
1045 Atmospheric Reanalysis Surface Products over the Ocean and Implications for Uncertainties in Air-
1046 Sea Boundary Forcing. *Journal of Climate*. 26. 153-170. 10.1175/JCLI-D-12-00090.1.
- 1047 Large, W.G., Yeager, S.G. (2009). The global climatology of an interannually varying air–sea flux
1048 data set. *Clim Dyn* 33, 341–364. 10.1007/s00382-008-0441-3